School of Geography, Earth and Environmental Sciences

Faculty of Science and Engineering

2024-04-26

The Geodynamic Significance of Continental UHP Exhumation: New Constraints From the Tso Morari Complex, NW Himalaya

Anna K. Bidgood *University of Oxford*

Andrew J. Parsons *School of Geography, Earth and Environmental Sciences*

Nick M.W. Roberts *British Geological Survey*

Dave Waters *University of Oxford*

Simon Tapster *University of Plymouth*

et al. *See next page for additional authors*

Let us know how access to this document benefits you

Authors

Anna K. Bidgood, Andrew J. Parsons, Nick M.W. Roberts, Dave Waters, Simon Tapster, and Phillip Gopon

The Geodynamic Significance of Continental UHP Exhumation

Bidgood, Anna K.; Parsons, Andrew J.; Roberts, Nick M.W.; Waters, Dave; Tapster, Simon; Gopon, Phillip

Document version:
Publisher's PDF, also known as Version of record

Link:
Link to publication in PEARL

Citation for published version (APA):

Correspondence to:

A. K. Bidgood,
akbidgood@gmail.com

The Geodynamic Significance of Continental UHP Exhumation: New Constraints From the Tso Morari Complex, NW Himalaya

Anna K. Bidgood[1] , **Andrew J. Parsons**[2] , **Nick M. W. Roberts**[3] , **Dave Waters**[1,4] , **Simon Tapster**[2] , **and Phillip Gopon**[5]

[1]Department of Earth Sciences, University of Oxford, Oxford, UK, [2]School of Geography, Earth and Environmental Sciences, University of Plymouth, Plymouth, UK, [3]Geochronology and Tracers Facility, British Geological Survey, Nottingham, UK, [4]Museum of Natural History, University of Oxford, Oxford, UK, [5]Department of Applied Geosciences and Geophysics, Montanuniversität Leoben, Leoben, Austria

Abstract The burial and exhumation of continental crust to and from ultrahigh-pressure (UHP) is an important orogenic process, often interpreted with respect to the onset and/or subduction dynamics of continent-continent collision. Here, we investigate the timing and significance of UHP metamorphism and exhumation of the Tso Morari complex, North-West Himalaya. We present new petrochronological analyses of mafic eclogites and their host-rock gneisses, combining U-Pb zircon, rutile and xenotime geochronology (high-precision CA-ID-TIMS and high-spatial resolution LA-ICP-MS), garnet element maps, and petrographic observations. Zircon from mafic eclogite have a CA-ID-TIMS age of 46.91 ± 0.07 Ma, with REE profiles indicative of growth at eclogite facies conditions. Those ages overlap with zircon rim ages (48.9 ± 1.2 Ma, LA-ICP-MS) and xenotime ages (47.4 ± 1.4 Ma; LA-ICP-MS) from the hosting Puga gneiss, which grew during breakdown of UHP garnet rims. We argue that peak zircon growth at 47–46 Ma corresponds to the onset of exhumation from UHP conditions. Subsequent exhumation through the rutile closure temperature, is constrained by new dates of 40.4 ± 1.7 and 36.3 ± 3.8 Ma (LA-ICP-MS). Overlapping ages from Kaghan imply a coeval time-frame for the onset of UHP exhumation across the NW Himalaya. Furthermore, our regional synthesis demonstrates a causative link between changes in the subduction dynamics of the India-Asia collision zone at 47–46 Ma and the resulting mid-Eocene plate network reorganization. The onset of UHP exhumation therefore provides a tightly constrained time-stamp significant geodynamic shifts within the orogen and wider plate network.

Plain Language Summary Mountains such as the Himalayas are formed during the collision of continents. During this process, continents can be subducted to depths of over 100 km. This important process can be interpreted with respect to the timing and forces involved in the collision. This study presents data from the Tso Morari dome in the North-West Himalaya, which constrains the timing of continental subduction and return back to the surface. Comparison of this data with similar settings 450 km along the edge of the Indian continent suggests that this entire region of the North-West Himalaya underwent similar subduction-related processes at a the same time. We surmise that the arrival of buoyant continental crust to the subduction zone triggered the return of the subducted rocks back to the earth's surface. This also coincides with major changes in the tectonic behavior of the Himalaya at this time as well as reorganization of the tectonic plates further afield. Our study shows that the timing of the return of continental crust back to the earth's surface can be viewed as an important timestamp marking a period of change and may be linked to other tectonic events taking place at the same time.

1. Introduction

The exhumation of continental crust from ultra-high pressure (*hereafter referred to as "UHP exhumation"*) is an important yet poorly constrained orogenic process (Guillot et al., 2009; Hacker & Gerya, 2013; Warren, 2013). Many studies relate UHP exhumation to other orogenic processes such as a reduction in the slab-pull force during the subduction of continental crust, slab break-off, and/or onset of various modes of orogenic extension/collapse (e.g., Brun & Faccenna, 2008; Burov et al., 2014; Chen et al., 2022; Guillot et al., 2009; Hacker et al., 2010; Little et al., 2011; Yamato et al., 2008). As such, UHP exhumation in the rock record is often interpreted to signify an important shift in the tectonic and geodynamic regime of an orogen (e.g., Chen et al., 2022; Guillot et al., 2009; Hacker et al., 2010; O'Brien et al., 2001; Soret et al., 2021; Yamato et al., 2008), However, the exact relationships

Validation: Nick M. W. Roberts,
Dave Waters, Phillip Gopon
Writing – original draft: Anna
K. Bidgood, Andrew J. Parsons
Writing – review & editing: Anna
K. Bidgood, Andrew J. Parsons, Nick
M. W. Roberts, Dave Waters

between continental UHP exhumation and the geodynamics of orogenesis and plate tectonics, as well as the mechanisms that facilitate this process, remain poorly constrained due to the difficulty of investigating UHP metamorphism and exhumation from the bedrock record (Hacker & Gerya, 2013; O'Brien, 2019; Warren, 2013). To better understand the processes of continental UHP exhumation and its impacts on orogenesis and plate tectonics, we must combine petrology-based pressure-temperature (P-T) pathways with radioisotope geochronological constraints. This approach allows us to determine the timing and rates of UHP exhumation through P-T space and with respect to the orogeny. However, such attempts to constrain the timing and rates of UHP exhumation are always complicated by the uncertainty with which accessory phase ages are related to P-T paths (e.g., Kohn et al., 2017; O'Brien, 2019a). This problem is clearly demonstrated in the UHP Tso Morari Complex of the NW Himalaya (Epard & Steck, 2008; Guillot et al., 2008; Steck et al., 1998), which forms the central study region of our investigation.

The Tso Morari Complex is one of two UHP terranes in the NW Himalaya, the other being the Kaghan Valley Complex, located ~450 km to the west of Tso Morari (Buchs & Epard, 2019; Epard & Steck, 2008; Guillot et al., 2008; O'Brien et al., 2001; Parrish et al., 2006; Steck et al., 1998). Over the last three decades, geochronological studies of Tso Morari have yielded a range of estimates for the timing of UHP metamorphism and exhumation, spanning a period of 11 Ma (Donaldson et al., 2013; Leech et al., 2007; St-Onge et al., 2013). Early interpretations were based on a limited number of spot analyses of zircon (e.g., $n = 19$, Leech et al., 2007), whereas the later publication by Donaldson et al. (2013) provided a more robust record ($n = 108$) with a zircon age distribution ranging from 53 to 37 Ma, with a peak at 47–43 Ma that provied a substantially narrowed estimate of peak UHP metamorphism. In contrast, estimates from the Kaghan UHP eclogites are tightly constrained to ~46 Ma (Kaneko et al., 2003; Parrish et al., 2006; Zhang et al., 2022). From these constraints, a diverse but poorly constrained set of models have been proposed for the exhumation of Tso Morari and Kaghan Valley complexes (Boutelier & Cruden, 2018; Kylander-Clark et al., 2008; Möller et al., 2015; Schwartz et al., 2007).

The spread of ages for UHP metamorphism and exhumation in Tso Morari, could, reflect differences in analytical techniques and their inaccuracies, but a likely cause is also the difficulty and uncertainty associated with linking geochronological data with independently constrained metamorphic petrology (Foster et al., 2004; Kohn et al., 2017; O'Brien, 2019a). This problem is compounded further in the Tso Morari complex because UHP rocks exist as meter-scale eclogite facies mafic pods hosted within amphibolite facies felsic gneiss. Accessory phases suitable for geochronology are rare in eclogite pods, so some studies have attempted to relate the P-T evolution of eclogite pods with geochronological constraints from the amphibolite facies gneiss (St-Onge et al., 2013). However, this approach carries additional uncertainties surrounding the structural and metamorphic relationships between the eclogite pods and the amphibolite facies gneiss in which they are hosted (O'Brien, 2019b).

To overcome these problems, estimates of the timing of UHP exhumation are better resolved using a combination of modern petrochronology techniques (Kohn et al., 2017), and where mineral size and zonation allows, high precision techniques (Parrish et al., 2006). The former can utilize a range of approaches, including: (a) the combination of geochronology, trace element geochemistry and metamorphic petrology, to quantitatively relate precise ages to specific stages on a metamorphic P-T path (e.g., Rubatto, 2002; Rubatto & Hermann, 2003); and (b) identifying and selecting a range of accessory phases associated with different metamorphic assemblages and lithologies, which collectively span a wide range of closure temperatures (Lotout et al., 2018; Regis et al., 2016; Tual et al., 2022). Such techniques provide the best opportunity to accurately and precisely constrain the timing of UHP exhumation.

In this study, we employ a range of petrochronological techniques to precisely constrain the timing of UHP metamorphism and exhumation of the Tso Morari Complex. We use detailed petrographic analyses, including major and trace element X-ray maps of garnet, to identify and relate prograde, peak, and retrograde metamorphic assemblages in mafic eclogite samples and amphibolite facies felsic gneiss samples (the Puga gneiss). This allows us to select a variety of accessory phases from different metamorphic assemblages for U-Pb geochronology, to constrain the timing of metamorphism at different points of the P-T path. Using laser ablation inductively coupled plasma mass spectrometry (LA-ICP-MS), we analyze zircon and rutile from an eclogite pod sample, and zircon, rutile, and xenotime from a felsic gneiss sample to constrain the timing of prograde, peak, and retrograde metamorphism. In addition, we analyzed zircon from the eclogite using chemical abrasion isotope dilution thermal ion mass spectrometry (CA-ID-TIMS) to more precisely constrain the timing of zircon crystallization.

Our results suggest that the onset of exhumation of Indian continental crust from UHP conditions occurred synchronously across the Tso Morari complex and Kaghan Valley complex at ~47–46 Ma.

1.1. The Geodynamic Significance of UHP Exhumation

After presenting our new geochronology data and interpreting its implications for the metamorphic evolution of the Tso Morari complex, we then consider the geodynamic implications of our new constraints for the Himalayan orogeny and the wider tectonic plate network. The early stages of continental collision involve a shift in the geodynamics of subduction due to the positive buoyancy of continental crust on the down-going plate (Afonso & Zlotnik, 2011; Capitanio et al., 2015; Hacker & Gerya, 2013; Laik et al., 2022; Warren, 2013). The exhumation of continental crust from UHP conditions provides an important marker of this geodynamic shift, due to the association of UHP exhumation with modification(s) to the subduction dynamics of a collision zone such as slab break-off, a reduction in slab dip, and/or an increase in mechanical coupling between the upper and lower plates (e.g., Afonso & Zlotnik, 2011; Chen et al., 2022; Guillot et al., 2008; Warren, 2013). The timing of UHP exhumation is especially important, as this constraint allows scientists to interpret the structural, metamorphic, and magmatic evolution of orogenesis with respect to changes in the subduction dynamics of a collision zone and vice-versa, offering an invaluable opportunity to test geodynamic and plate tectonic models of continental collision against bedrock constraints (e.g., Capitanio et al., 2015; Chen et al., 2022; Guillot et al., 2008; Yamato et al., 2008).

More broadly, the timing of continental UHP exhumation can be used to better understand the impacts of continental collision on tectonic plate networks. Continental collisions change the summative slab pull forces within their encompassing plate network, either by reducing slab pull of the collision zone during subduction of buoyant continental lithosphere or by removing slab pull from the collision zone altogether via slab break off (e.g., Afonso & Zlotnik, 2011; Capitanio et al., 2015; Chen et al., 2022; Laik et al., 2022). In some cases, this can trigger a plate network reorganization event, defined by a short period (~10–20 Myr) of rapid and widespread modifications to the speed and direction of tectonic plate motions and the topology of plate boundaries (e.g., Gibbons et al., 2015; Gürer et al., 2022; Matthews et al., 2012; Müller et al., 2016). Understanding the causes and occurrences of these reorganizations is important as they can drastically alter the course of Earth's paleogeographic and tectonic evolution in a relatively short period of time.

Our understanding of plate network reorganizations is limited due to the difficulty of robustly demonstrating a causative relationship between temporally overlapping, but spatially disparate tectonic events and coeval changes in plate kinematics. This is particularly problematic when investigating reorganizations associated with continental collision, due to the complexity of their bedrock record and the uncertainties of geochronological constraints that obfuscate the duration and order of localized events and their geodynamic relationships with network-wide modifications of plate kinematics. Faced with this problem, constraints such as the timing of UHP exhumation, which directly correspond to changes in subduction dynamics of a collision zone, can provide crucial geochronological markers for constraining causative relationships between collisions and plate network reorganizations (e.g., Gibbons et al., 2015; Matthews et al., 2012).

A major plate network reorganization for the Indian, Eurasian, African, Australian, and Antarctic plates is recognized by previous studies during the Eocene (Gibbons et al., 2015). This reorganization is arguably associated with the Himalayan orogeny (Gibbons et al., 2015; Zahirovic et al., 2016), but uncertainty in the collision history of the orogeny (e.g., Hu et al., 2016; Kapp & DeCelles, 2019; Parsons et al., 2020; van Hinsbergen et al., 2019) means that a precise and unambiguous timestamp linking the bedrock record of the orogen with the Eocene plate network reorganization has been lacking. It is therefore unclear exactly how the structural and metamorphic evolution of the Himalayan orogeny relates to and/or caused plate kinematic changes during the Eocene reorganization. Our new, precise geochronometric constraints for the UHP exhumation in the NW Himalaya present a valuable opportunity to evaluate the temporal relationships between the Himalayan orogeny and the Eocene plate network reorganization and consider their causative links. With the modern advent of the user-friendly GPlates plate reconstruction application (Müller et al., 2018), similar integrated analyses of collisional metamorphism and plate kinematics could be used to better understand the plate tectonic consequences of other orogenies.

2. Geological Background

2.1. The Himalayan Orogeny and the India-Asia Collision: Definitions

In order to interpret our data with respect to the Himalayan orogeny and India-Asia collision, it is necessary to outline some definitions used hereafter. Working hypotheses for tectonic formation of the Himalayan orogeny and the India-Asia collision can be broadly categorized into "Single Collision" and "Double Collision" models (e.g., Hu et al., 2016; Kapp & DeCelles, 2019; Parsons et al., 2020). Single Collision models propose a single continental collision between India and Eurasia, beginning at ∼61 Ma (An et al., 2021) with convergence and under thrusting continuing to the present day (e.g., Gansser, 1966; Hu et al., 2016; Ingalls et al., 2016; Le Fort, 1975). Such models are not considered tenable as they require extreme volumes of continental subduction and do not adequately explain the significant kinematic and geodynamic changes which occur within the orogen and the surrounding plate network between 50 and 40 Ma (e.g., Parsons et al., 2020, 2021; van Hinsbergen et al., 2019). As such, the results of this study are interpreted in the context of the competing "Double Collision" models, for which two alternative working hypotheses exist, differing with respect to the nature of the first collision. In both hypotheses, "first collision" began at ∼61 Ma (e.g., An et al., 2021; Hu et al., 2015) but corresponds, to either (a) collision of the Indian continent with an equatorial Neotethys intra-oceanic arc (e.g., Bouilhol et al., 2013; Burg & Bouilhol, 2019; Patriat & Achache, 1984; Replumaz et al., 2014; Stampfli & Borel, 2004); or (b) collision between an India-derived *microcontinent* and the Eurasian active margin (e.g., Sinha Roy, 1976; van Hinsbergen et al., 2019; Zhou & Su, 2019). "Second collision" occurred between the Indian continent and the Eurasian active margin sometime between 50 and 25 Ma (e.g., Burg & Bouilhol, 2019; Parsons et al., 2021; Patriat & Achache, 1984; Replumaz et al., 2014; Searle, 2019; van Hinsbergen et al., 2019).

In the context of these double collision models, the Himalayan orogeny corresponds to the deformation of Indian continental crustwhich initiated during first collision and continued through second collision. In contrast, the "India-Asia collision" sensu-stricto corresponds to the second collision event only (e.g., Parsons et al., 2020, 2021). Debate continues to surround the relative validity of the two "double collision" hypotheses and further considerations can be found in recent reviews (e.g., Kapp & DeCelles, 2019; Parsons et al., 2020; Searle, 2019; van Hinsbergen et al., 2019); our study is presented in the context of both double collision models (e.g., Burg & Bouilhol, 2019 vs. van Hinsbergen et al., 2019) as it is beyond the scope of the new data presented in this paper to address their relative validity.

2.2. Geology of the Tso Morari Complex

The Tso Morari dome is situated on the north-western margin of the Indian plate (Figure 1), and is separated from the Ladakh batholith of the Asian plate located to the north by the Indus suture zone (Fuchs & Linner, 1996). The Tso Morari dome comprises a set of stacked nappes, folded into a northwest-southeast trending periclinal antiform (Buchs & Epard, 2019; Steck et al., 1998). The structurally lowermost nappe is the Tso Morari Complex (also known as the Tso Morari Gneiss, Epard & Steck, 2008), which crops out in the center of the dome. The Tso Morari Complex contains Ordovician granite and disrupted mafic dykes and sills intruded into Cambrian sediments of the Indian continent. Granitic rocks are variably deformed, resulting in an array of undeformed metagranites, augen gneiss and garnet-mica-schists within the Tso Morari Complex. The range of deformation states preserves different parts of the P-T-t history of the Tso Morari Complex. The early subduction-related history is rarely preserved except as thin corona textures in low strain metagranite (Bidgood et al., 2023), whereas the high strain gneisses are often overprinted by later, amphibolite facies metamorphism and exhumation-related deformation. These end-member states are distinguished locally as the Polokongka La granite and the Puga Gneiss, which share the same granitic protolith, and differ only in their state of strain and metamorphic evolution (Girard & Bussy, 1999).

Mafic rocks within the Tso Morari complex locally preserve eclogite-facies mineral assemblages formed at conditions of >26 kbar, 500–645°C (e.g., Bidgood, 2020; de Sigoyer and Guillot, 1997; Guillot et al., 1997; St-Onge et al., 2013). Evidence of high-pressure metamorphism is rarely observed in the felsic metagranitoid rocks but has been recorded by glaucophane-bearing metasediments (Guillot et al., 1997), pseudomorphs after coesite within the Polokongka La granite (Bidgood, 2020) and thin corona textures (garnet, phengite, ilmenite) and pseudomorphs (kyanite, garnet and phengite) after cordierite in low strain metagranites (Bidgood et al., 2023). Later overprinting at amphibolite-facies conditions is recorded in the retrogressed eclogites at 610 ± 30°C at
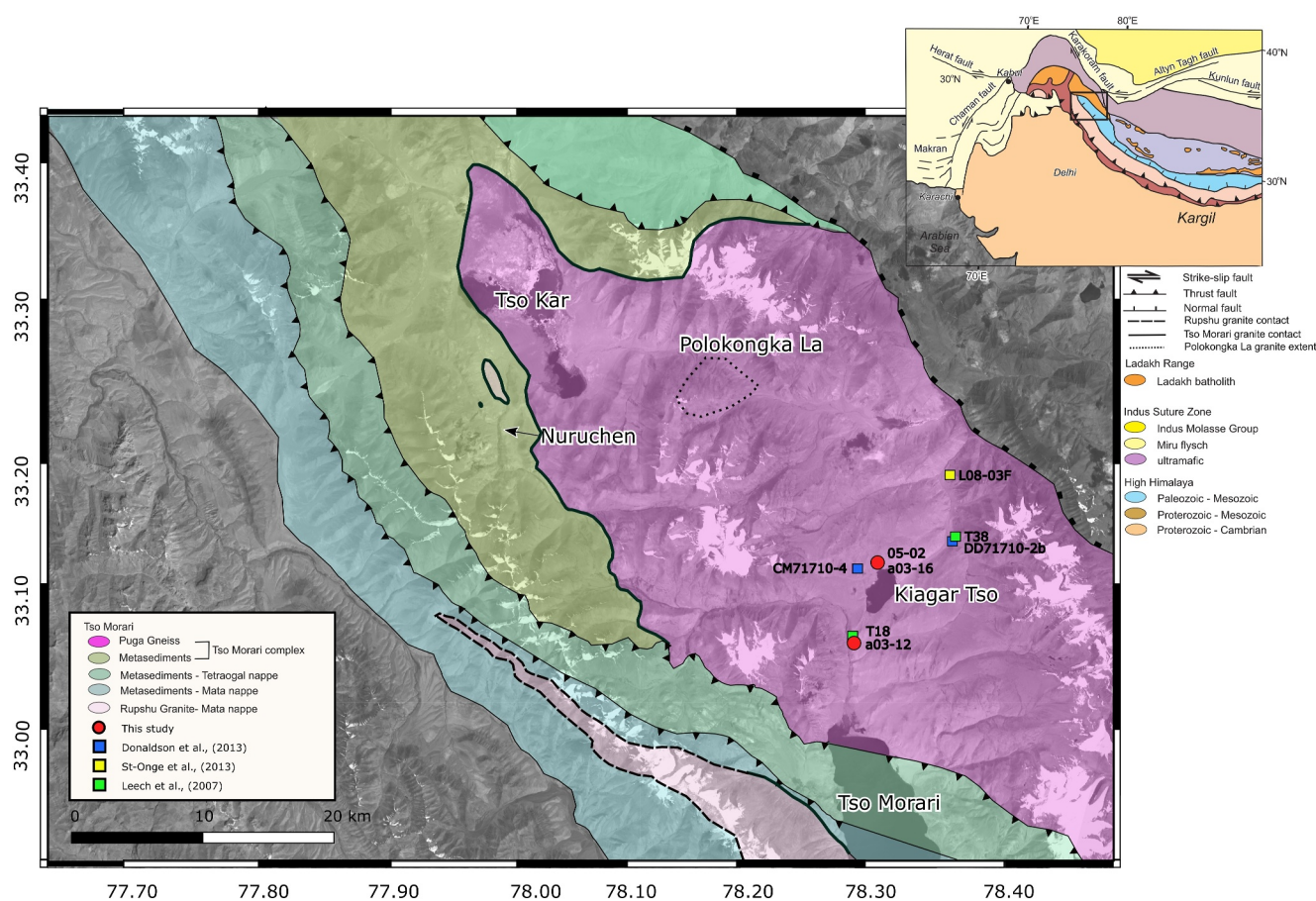
Figure 1. Geological map adapted from Epard and Steck (2008), St-Onge et al. (2013), and references therein, showing location of geochronological samples. Background USGS landsat data downloaded from https://earthexplorer.usgs.gov/. Coloring corresponds to bands 762, greyscale by luminosity.

9 ± 3 kbar (Guillot et al., 1997) and in the felsic rocks at 650 ± 50°C at 9 ± 1 kbar (Girard, 2001), 630°C ± 30°C at 9 ± 2 kbar (Guillot et al., 1997) and 725 ± 50°C at 7.1 ± 1.0 kbar (St-Onge et al., 2013).

This study describes the record of subduction-related major and accessory mineral growth preserved in a rare garnet-bearing Puga Gneiss which records a part of the P-T-t history not preserved elsewhere. Additionally, new data is presented which tightly constrains zircon growth in the mafic eclogites, which, in conjunction with the observations in the Puga Gneiss, allows us to place the petrographic observations in a geochronologic and geodynamic context.

2.3. Geochronology of the Tso Morari Complex

The range of estimates for UHP metamorphism and exhumation in the Tso Morari complex (54–44.5 Ma, Donaldson et al., 2013; Leech et al., 2007; St-Onge et al., 2013) is less tightly resolved than the age estimates for Kaghan (~46 Ma, Kaneko et al., 2003; Parrish et al., 2006; Zhang et al., 2022). Given the differences in analytical techniques used to date the Tso Morari complex and the difficulty in relating these dates to metamorphic stages, it remains unclear to what degree the spread of ages from Tso Morari can be assigned to geological heterogeneity or to analytical uncertainty and artifacts. For example, the absence of petrographic context in some studies makes it difficult to interpret the age clusters with respect to specific metamorphic conditions (see O'Brien, 2006 for further discussion). Additionally, the link between zircon growth and fluid infiltration (e.g., Chen & Zheng, 2017; Chen et al., 2010; Kohn et al., 2015; Sheng et al., 2012; Skuzovatov et al., 2021) has not been explored in the context of the published data. Importantly, given the types of data yielded from Tso Morari thus far (see following summary), it is not possible to robustly constrain whether zircon growth in the mafic eclogites was prolonged or punctuated, and whether the range of dates correspond to prograde, peak and/or retrograde metamorphic

conditions. Given the narrow age range for UHP metamorphism from Kaghan only 450 km away, comparative age estimates from Tso Morari would have significant implications for the processes of continental subduction and UHP exhumation; as such, this is the primary motivation for this study. Here we present new and precise ages of eclogite-facies metamorphism that can be compared with the ages recorded at Kaghan, along with new in situ data which, when combined with the petrographic interpretation, records an additional petrographic age and stage of the evolution of the Tso Morari complex that has not been previously observed.

The Puga Gneiss and Polokongka La granite contain zircon with thin metamorphic rims surrounding igneous cores, with the latter dated by U-Pb at 479 ± 1 Ma (Girard & Bussy, 1999; Leech et al., 2007). Initial estimates of the age of high pressure metamorphism by De Sigoyer et al. (2000) used Lu-Hf isochron ages on garnet-clinopyroxene-whole-rock data, Sm-Nd on garnet-glaucophane-whole-rock data, and U-Pb in allanite, giving ages of 45 ± 4.4, 55 ± 12.0, and 55 ± 17.0 Ma, respectively. These estimates attempted to date minerals which can definitively be linked to metamorphic reactions/conditions, but this was hindered by the large uncertainties on these dates.

A spread in zircon dates from 55 to 45 Ma was recorded in the Puga Gneiss by Leech et al. (2007) by U-Pb SHRIMP dating of the metamorphic rims found around igneous zircon grains ($n = 19$; 4 ages interpreted). Sub-concordant data were split into groups arbitrarily (see O'Brien, 2006), and interpreted to represent ultrahigh-pressure metamorphism at 53.3 ± 0.7 Ma, followed by further zircon growth in eclogite facies conditions at 50.1 ± 0.6 Ma, amphibolite facies at 47.5 ± 0.6 Ma, and a lower temperature growth at 45.2 0.7 Ma. St-Onge et al. (2013) recorded monazite and allanite U-Pb SHRIMP ages of 45.3 ± 1.1 and 43.3 ± 1.1 Ma respectively, interpreted to represent post-eclogite facies peak temperature metamorphism of 7.0–8.4 kbar at 705–755° C, based on pseudosection modeling of the observed garnet breakdown reaction. Cooling through phengite, biotite and muscovite Ar-Ar closure temperatures is recorded at 48.0 ± 2.0, 31.1 ± 0.3, and 29.3 ± 0.3 Ma (De Sigoyer et al., 2000) respectively, with further cooling recorded by apatite and zircon fission track data at ~23.5–7.5 Ma (Schlup et al., 2003). Dates from within the Puga Gneiss are dominated by post-peak, amphibolite facies ages recording Barrovian metamorphism, cooling and uplift.

The mafic eclogites better preserve the early high-pressure metamorphic history in their major and accessory mineral assemblages. St-Onge et al. (2013) analyzed zircon in situ with SHRIMP U-Pb geochronology, yielding an age of 58.0 ± 2.2 Ma ($n = 2$) for zircon included in the core of a garnet, and 50.8 ± 1 Ma ($n = 4$) for zircon included/adjacent to matrix barroisite, phengite and garnet. The older age is interpreted to record zircon crystallization during prograde garnet growth to high pressure, and the younger age is interpreted to represent peak metamorphism in the eclogite facies. Whilst the St. Onge et al. (2013) study provides a textural constraint on the prograde zircon ages which was previously unknown, the data include a limited number of spots and the presence of common lead. Donaldson et al. (2013) used in situ split-stream LA-ICP-MS to measure U-(Th)-Pb combined with REE concentrations of zircon from two mafic eclogites, located ~10 km apart. Lower intercept dates of each sample overlap at 45.3 ± 1.6 and 44.2 ± 1.2 Ma. These ages broadly overlap with that of Kaghan, as highlighted by Donaldson et al. (2013), but these authors also argue for protracted zircon crystallization in the eclogite facies (ca. 47–43 Ma) based on the spread of single spot dates and consistent REE signatures with an absence of an Eu anomaly and flat HREE profiles. The Donaldson et al. (2013) results improve upon the constraints of St. Onge et al. (2013) based on the number of data, but are still hampered by both the presence of common lead and the precision of the in situ method which yields single spot uncertainties of ca. 1–10 Ma.

The age of UHP metamorphism in the Kaghan Valley Complex has been estimated using U-Pb SHRIMP and U-Pb ID-TIMS analyses of zircon from eclogite-facies mafic rocks, yielding ages of 46.2 ± 0.7 Ma (Kaneko et al., 2003) and 46.4 ± 0.1 Ma (Parrish et al., 2006), respectively. These zircons were found included in UHP garnet rims with coesite inclusions. Eclogite facies ages of zircon and allanite from Kaghan were also estimated using U-Pb and Th-Pb ID-TIMS analyses at 45.5 ± 6.6 and 46.5 ± 1.0 Ma, respectively (Parrish et al., 2006). An additional age of eclogite facies zircon was estimated using U-Pb SIMS at 46 ± 2 Ma in Naran, 30 km south-west of Kaghan (Zhang et al., 2022). A compilation of geochronology of high pressure metamorphism in the north west Himalaya can be found in Supporting Information S1 and is compared to our new data in Figure 8.

3. Petrography

3.1. Analytical Methods

Petrographic study of 29 mafic eclogites and 28 Puga Gneiss samples from the Tso Morari Complex was undertaken, with one fresh eclogite (a03-16), one retrogressed eclogite (a03-12) and one gneiss sample (05-02) selected for further petrological analyses. Major element compositions of minerals that exhibit solid solutions were measured using a Cameca SX-5 field emission electron microprobe at the University of Oxford, with a 15 kV acceleration potential, 20 nA beam current, 30 s count time per major element (30 s background) and 60 s count time on Ti (60 s background). A range of natural and synthetic oxide standards were used including albite (Na, Al, Si), Orthoclase (K), MgO (Mg), wollastonite (Ca), andradite (Fe), Mn metal (Mn), and synthetic TiO_2 (Ti) and analyses were verified against secondary mineral standards. Mineral spot analyses and line profiles were taken across garnet to determine the extent of intracrystalline compositional variation (see Supporting Information S1).

Quantitative major element X-ray maps of garnets were collected from polished thin sections using the CAMECA SX-5 field emission electron microprobe at the University of Oxford at a working distance of 10 mm, a 15 k V acceleration potential, 170 nA current, 0.06 s dwell time and a 3 μm step size for the elements P, Ca, Mn, Mg, and Fe. A dwell time of 0.032 s and a 200 nA beam current were used for the elements Al, Si, Ti, Y, and Yb. A range of natural and synthetic oxide standards were used including Durango apatite (P), andradite (Ca, Fe), Mn metal (Mn), MgO (Mg), albite (Al, Si), TiO_2 (Ti), Y metal (Y), Yb metal (Yb).

3.2. Petrography and Petrology: Observations

3.2.1. Puga Gneiss (Sample 05-02)

Puga Gneiss sample 05-02 was collected from the north shore of Kiagar Tso (33.1214°N, 78.2958°E), in the middle of the Tso Morari Complex. Sample 05-02 is a strongly foliated, garnet-bearing gneiss comprising albite, quartz, muscovite, biotite and garnet, with accessory zircon, apatite, rutile, and xenotime. Sample 05-02 shows a schistosity (S2) defined by bands of white mica, albite and quartz (Figure 2a) which wrap around larger garnet porphyroblasts. Quartz occurs in polycrystalline ribbons or lenses separated by narrow bands of white mica, indicative of a high-strain fabric (Figures 2a–2d). The quartz ribbons are cut by discontinuous shear bands forming an S-C′ fabric. Quartz grains are >200 μm and equant with ameboid shapes along grain boundaries indicative of grain boundary migration (GBM) dynamic recrystallization (e.g., Stipp et al., 2002). Albite bands and lenses are largely composed of fine-grained aggregates. Among these, larger feldspar grains show subgrains of similar size to the dominant population, suggesting that dynamic recrystallization occurred in the subgrain rotation (SGR) regime for feldspar (Passchier & Trouw, 2005). Zircon and rutile occur in the matrix.

Garnet porphyroblasts of varying size are scattered through the rock. They are abundantly fractured, and partly replaced by biotite, white mica and chlorite. The studied section contains one large (6 × 5 mm) ovoid garnet porphyroblast (Figure 3) that contains significant textural complexity (see below). Fine-grained inclusion trails of quartz and rutile define a primary foliation (S1), which is oblique to the matrix fabric (S2) and folded at the core-rim boundary (Figure 3a). Kyanite occurs within the garnet core, adjacent to staurolite, surrounded by white mica (Figure 3a). The garnet is subhedral with embayments containing biotite, white mica and xenotime (Figure 3a).

Garnet exhibits concentric zonation, comprising three distinct zones (Figure 3). The garnet core (zone P1, Figure 3c) has an approximately uniform composition of $Alm_{79.0}Grs_{12.5}Pyr_{5.5}Spss_{4.0-2.3}$. Inclusions of quartz, rutile and white mica are found throughout zone 1, whereas inclusions of kyanite are restricted to the inner portion of zone P1 (Figures 3a–3f). Zone P2 (Figures 3b, 3d, and 3f) is marked by a decrease in Ca and increase in Mn. It contains a narrow annulus of high Y content, and its outer boundary is faceted. The narrow rim zone P3 (Figures 3d and 3f) shows a marked increase in Mg (to 16% pyrope) and Ca (to 13% grossular), with lower Mn. It is discontinuous around the garnet margin. Zones P2 and P3 contain quartz, white mica, and rutile inclusions, but to a lesser extent than in zone 1. Kyanite is absent from zones P2 and P3. In zones P1 and P2, magnesium-enriched haloes are developed along the internal fracture network, surrounding many larger inclusions of white mica and quartz, and connecting with the outer zone of the garnet.
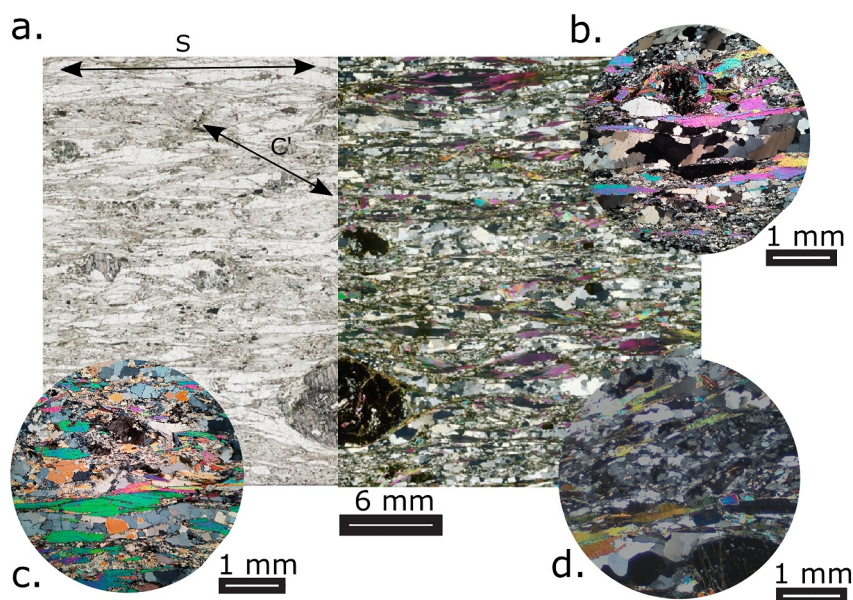
Figure 2. (a) Puga Gneiss Sample 05-02. PPL and XPL image showing gneissose texture consisting of quartz-rich, feldspar-rich and mica-rich layers. Large garnet wrapped by fabric (S2) shown in Figure 3. (b and c) Puga Gneiss Sample 05-01, adjacent to 05-02. (b) Polycrystalline quartz-rich band in between mica sheets. Recrystallized quartz shows undulose extinction. Quartz grains in the lower part of the image span the width of the mica ribbons. (c) Stacked white mica sheets curve into high strain fabric showing top to the right sense of shear. Annealed quartz band and dusty albite and apatite present. (d) Puga Gneiss Sample 05-02. Fine-grained albite lens between mica sheets.

3.2.2. Mafic Eclogite (Sample a03-16)

Sample a03-16 is a mafic eclogite taken from the same locality as Puga Gneiss sample 05-02 (33.1214°N, 78.2958°E), adjacent to sample CM71710-4 of Donaldson et al. (2013), and displays similar features to mafic eclogites described from other localities in the Tso Morari Complex (e.g., Jonnalagadda et al., 2017; O'Brien & Sachan, 2000; Palin, Searle, et al., 2014; Palin, St-Onge, et al., 2014; St-Onge et al., 2013; Wilke et al., 2015). Sample a03-16 has a medium- to coarse-grained granoblastic texture with a major mineral assemblage of garnet, omphacite, phengite, quartz, and talc, with minor amounts of clinozoisite, amphibole, carbonate, rutile, and zircon.

Garnet and omphacite (Figure 4a) are in textural equilibrium, forming planar contacts, with coarse grained homogeneous phengite and talc. In some places, symplectites after omphacite are observed, comprised of amphibole, plagioclase and occasional diopside. Dolomite is also present in the matrix as large poikiloblasts containing inclusions of phengite, omphacite and rutile.

Amphibole occurs in the matrix and as inclusions in garnet (Figure 4b). In common with other sampled outcrops, coarse-grained matrix amphibole typically has pale green winchite cores, zoned toward a pargasitic composition at rims. Thin mantles of green pargasitic amphibole surround garnet, and amphibole inclusions in garnet are darker blue-green pargasite and ferroparagasite. Fine-grained intergrowths of biotite and plagioclase surround phengite. Matrix quartz and omphacite contain clusters of zircon inclusions, whereas garnet, omphacite, quartz, phengite, and talc contain rutile inclusions (Figure 4c). Garnet occurs as subhedral porphyroblasts that are 3–4 mm in diameter (Figure 4b) and contain inclusions of zoned blue-green amphibole, and also quartz and rutile. Rutile commonly forms angular clusters of grains, both in the matrix and within garnets, which we interpret as replacing a former igneous Fe-Ti oxide.

Major and trace element maps of a single garnet in sample a03-16 show three zones (Figure 5). Zone E1 (Figure 5d) defines the core region, which has a composition of Alm48-42 Grs24-29 Pyr20-30 Sps6-1, with increasing almandine and pyrope components from core to rim (Figures 5b and 5c). The rim of the zone E1 core is outlined by a Mn-rich annulus. Zone E2 surrounds the zone E1 core and is defined by a calcium trough with a faceted outline (Figures 5d and 5e). Zone E3 (Figure 5b) forms along the garnet rim defined by a Mg-rich, Mn-
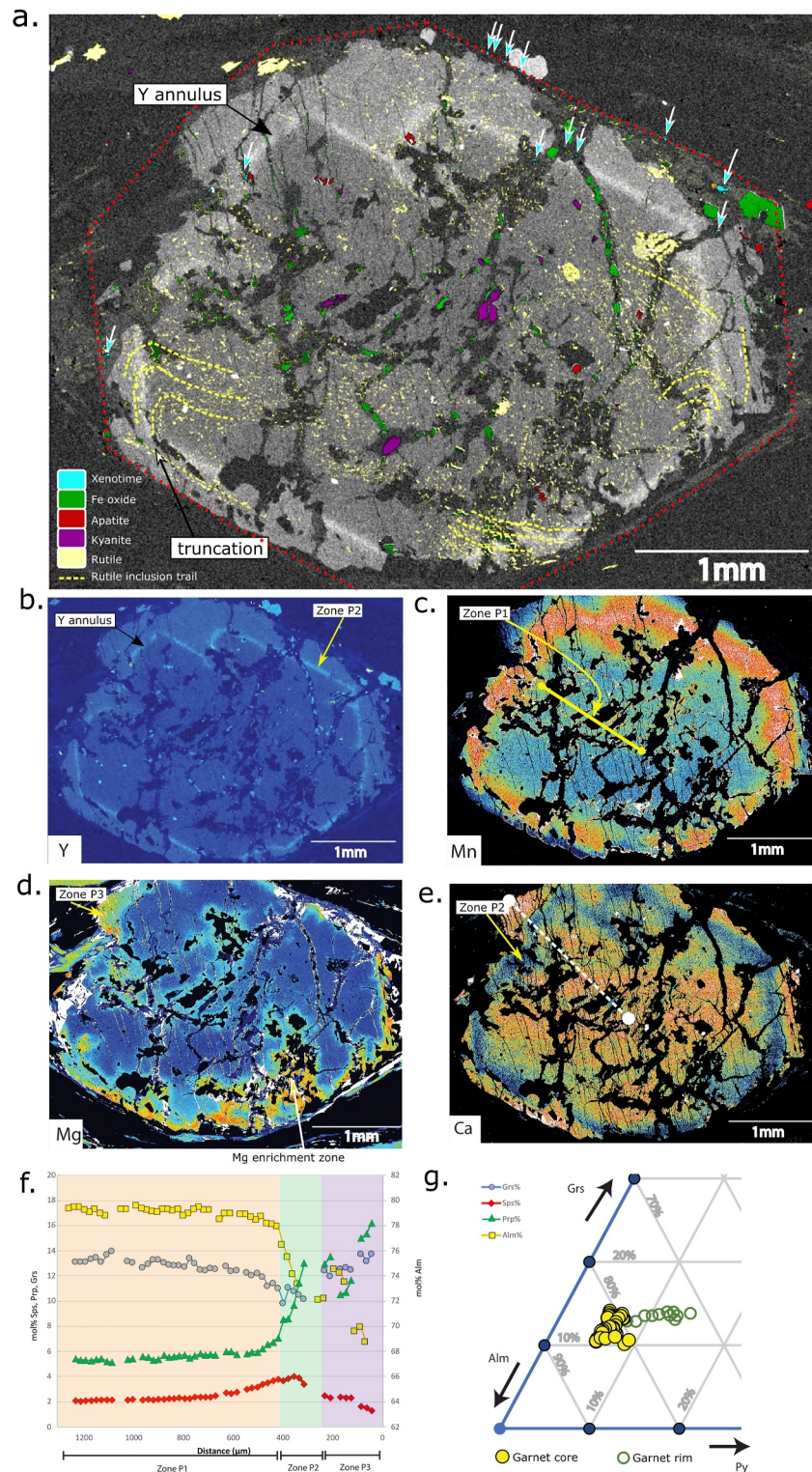
Figure 3. Puga Gneiss Sample 05-02 garnet. (a) The brightest grains from the Ti map (yellow), Ca map (red), Fe map (green), Y map (cyan) and Al map (purple) are overlain on an Y map adjusted for Y-zonation in garnet. The location of xenotime grains can be identified based on the brightest Y locations to correspond with the micaceous rim after garnet. The map also highlights the orientation of rutile inclusion trails and the location of rectangular rutile clusters. The approximate outline of the original garnet is highlighted as a red dashed line. (b–e) Yttrium, manganese, magnesium and calcium EPMA element maps. Location of the core-rim boundary defined by the yttrium high. (f) Garnet zoning profiles from core (left) to rim (right). (g) Ternary diagram of transect across garnets. Approximate location of garnet transect shown by white dashed line on panel (e).
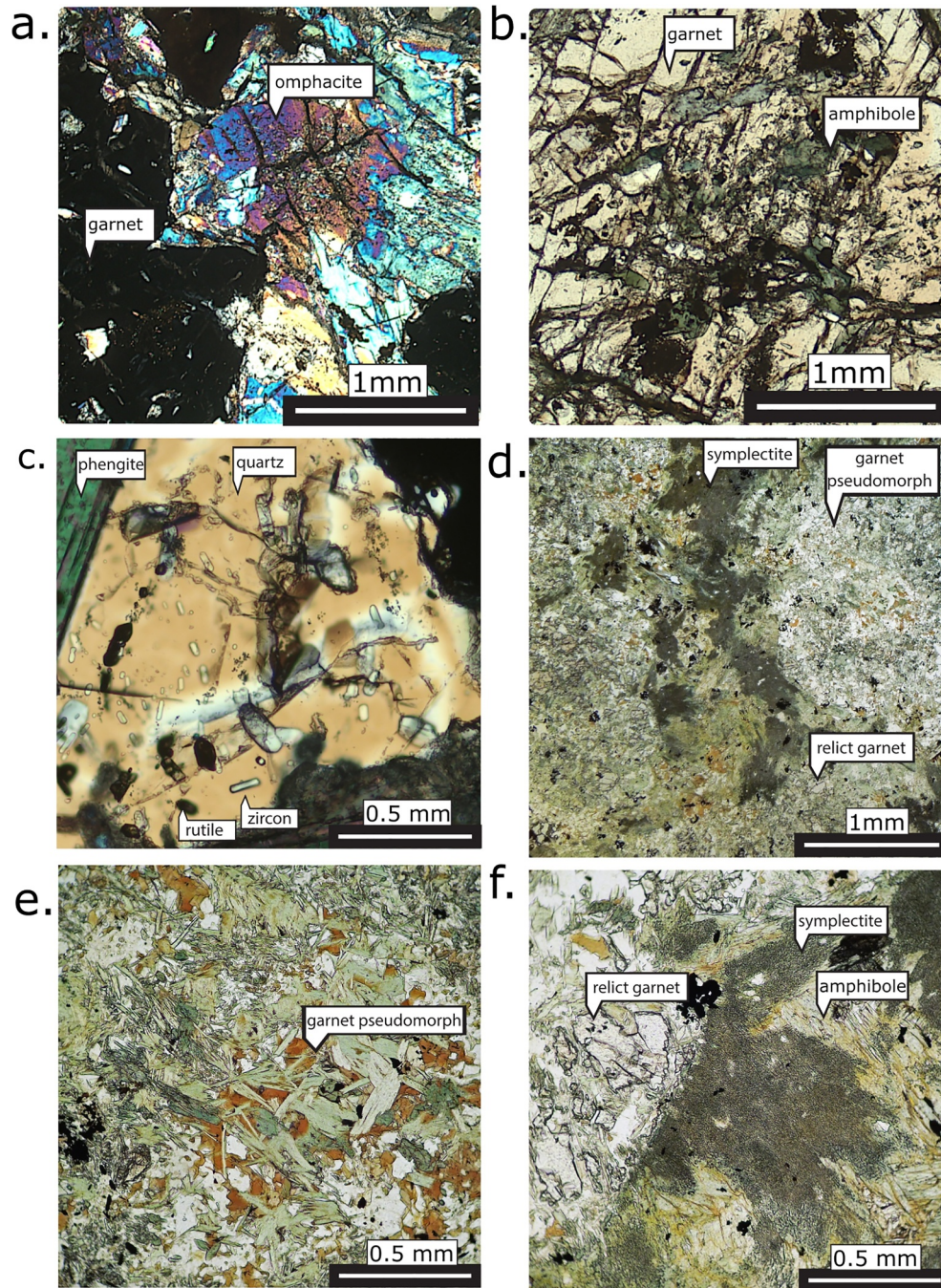
Figure 4. Photomicrographs of mafic eclogites. (a) Sample a03-16, XPL, poikiloblastic garnets and omphacite. (b) Sample a03-16, color zoning in garnet with amphibole inclusions ranging in color from blue to green. (c) Sample a03-16, matrix quartz with abundant high relief zircon and dark rutile inclusions. (d–f) Sample a03-12 retrogressed mafic eclogite. (d) Subhedral pseudomorphed garnets present on the edge of the image. Dark-colored, fine-grained intergrowth of plagioclase and amphibole (symplectite) after omphacite. Coarse-grained, green matrix amphiboles interlocked with omphacite pseudomorphs. (e) Core of large pseudomorphed garnet showing aggregate of chlorite, biotite and minor green amphibole set in plagioclase. (f) Dark amphibole-plagioclase symplectite after omphacite adjacent to partly pseudomorphed garnet.

poor rim with shows an increase in pyrope (to 30%–35%) and grossular (to 30%, decreasing to 16% at the outer rim). Mg- rich E3-like domains also extend in some places from the outer rim toward the core of the garnet, cutting across concentric garnet zones E1 and E2, and surrounding inclusions, often forming channelized features (Figures 5b and 5c).
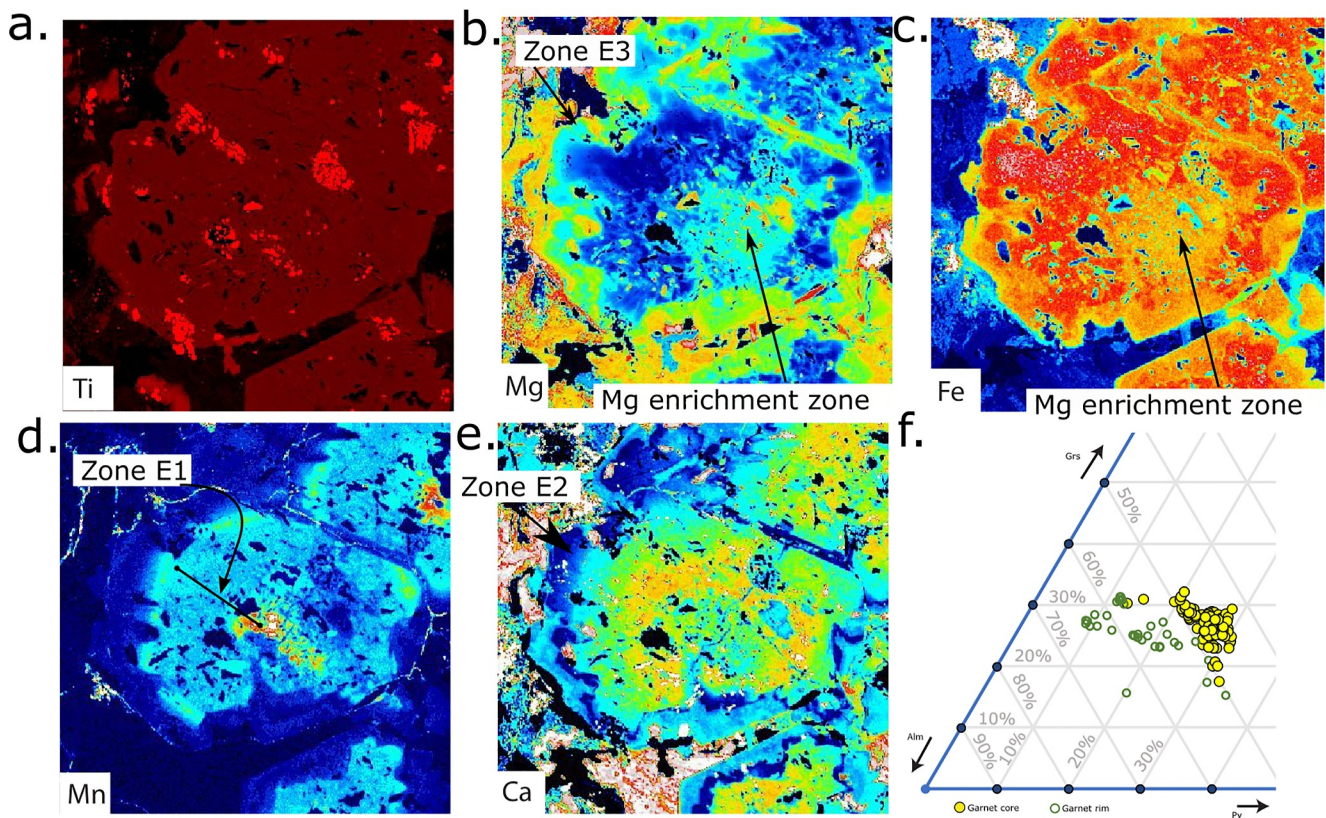
Figure 5. Garnet maps from mafic eclogite sample a03-16. (a) Ti map showing clusters of rutile inclusions forming distinct shapes after Fe-Ti oxides. b-e. Mg, Fe, Mn, and Ca maps showing concentric zoning patterns cut by Mg-Fe embayments emanating from the outside rim of the garnet. (f) Ternary diagram of transect across garnet showing Fe-Mg alteration and garnet rim.

3.2.3. Retrogressed Mafic Eclogite (Sample a03-12)

Sample a03-12, along with the adjacent sample a03-09, is a retrogressed mafic eclogite from "The Bridge" locality (33.0677°N, 78.2758°E), ~8 km south of sample a03-16. This is the same locality sampled and analyzed by Leech et al. (2007) (their sample T18). The sample is composed of garnet, amphibole, plagioclase, biotite, chlorite, ilmenite, rutile and zircon. Relict garnet is preserved within pseudomorphs that preserve subhedral garnet shapes, but are largely replaced by plagioclase, hornblende, biotite and chlorite aggregates (Figures 4d and 4e). Former matrix omphacite has been overprinted by coarse-grained blue-green sodic-calcic amphibole (cf. Palin, Searle, et al., 2014; Palin, St-Onge, et al., 2014), and subsequently pseudomorphed by fine-grained amphibole-plagioclase intergrowths (Figure 4f). Chlorite and biotite form aggregates which overprint the surrounding metamorphic patterns. Rutile grains occur in garnet and matrix amphibole, and are rimmed or replaced by ilmenite in retrogressed areas. Zircon occurs as small grains in the matrix.

3.3. Petrography and Petrology: Interpretation and Metamorphic Correlation

3.3.1. Puga Gneiss (Sample 05-02)

The Puga Gneiss (sample 05-02) displays evidence of two metamorphic assemblages. The first is defined by the garnet compositional zoning, and the inclusion suite of quartz, kyanite, rutile and zircon. Quartz and rutile inclusions define a crenulated primary foliation (S1). Kyanite is found exclusively within garnet. The garnet compositional zoning has features that match the zoning in eclogite garnet (cf. St-Onge et al., 2013; Figure 5), that is, a Ca-rich core (P1 = E1), Ca-poor trough (P2 = E2) and Mg- and Ca-rich rim (P3 = E3). This is consistent with prograde growth culminating in eclogite-facies conditions (e.g., O'Brien, 2019b; St-Onge et al., 2013; Wilke et al., 2015). The Mg distribution in the garnet interior implies that some fracturing occurred at near-peak conditions.

The second assemblage is defined by the rock matrix grains outside the garnet porphyroblasts, which form a segregated quartz-feldspar-mica mineral banding modified by an S-C′ fabric. Accessory minerals in this matrix assemblage include rutile and zircon. Dynamic recrystallization of quartz by grain boundary migration suggests a deformation temperature in excess of 530°C (Stipp et al., 2002), and evidence for subgrain rotation in albite is consistent with about 600°C (Passchier & Trouw, 2005). No lower-temperature dynamic recrystallization microstructures are observed, and minor chlorite, generally associated with garnet, is undeformed. Rutile is stable in the rock matrix, commonly enclosed in white mica. Based on these observations, we interpret the matrix assemblage to reflect metamorphism and deformation on the retrograde path, at amphibolite-facies conditions.

A distinct mineral association surrounds the large garnet in sample 05-02, where parts of the Mg-rich rim zone (P3) of the garnet are missing, due to partial resorption of garnet, and micaceous aggregates in embayments and fractures host xenotime grains (Figure 3a).

3.3.2. Mafic Eclogite (Sample a03-16)

Sample a03-16 contains three identifiable metamorphic assemblages. Garnet and omphacite (Figure 4a) in textural equilibrium with coarse grained homogeneous phengite and talc define a peak pressure eclogite-facies mineral assemblage (e.g., M2 of St-Onge et al., 2013). Accessory phases within this peak assemblage include zircon, present as clusters of grains included within matrix quartz and omphacite, and rutile, present as inclusions, commonly clustered, within garnet, omphacite, quartz, phengite, and talc (Figure 4c). Inclusions of zircon and rutile in garnet cores suggest that initial growth of these grains may have begun prior to eclogite facies metamorphism. Within garnet, the increase in pyrope component from core to rim, corresponds to garnet growth during prograde to peak eclogite conditions. We interpret zones E1–E3 as a prograde to peak assemblage, where zone E3 correlates with the omphacite, phengite and talc peak assemblage described above. The second metamorphic assemblage is defined by the early breakdown products of the peak assemblage phases. The dominant example is the zoned blue-green matrix amphibole, which may represent the product of talc dehydration as well as the influx of external fluids under eclogite-facies conditions (cf. Palin, Searle, et al., 2014; Palin, St-Onge, et al., 2014). The third assemblage includes feldspar-bearing symplectites after omphacite, and secondary fine-grained white mica aggregates forming in the irregular rims of coarse-grained phengite. These represent an amphibolite-facies overprint consistent with the matrix assemblage of Puga gneiss sample 05-02.

3.3.3. Retrogressed Mafic Eclogite (Sample a03-12)

Sample a03-12 is dominated by a post-peak metamorphic assemblage, whereas the peak assemblage displayed by sample a03-16, is identifiable in a03-12 as relict garnet grains and pseudomorphs after garnet and omphacite. Blue-green amphiboles are interpreted as an early post-peak phase, which grew within the eclogite facies field prior to the appearance of stable sodic feldspar during decompression (e.g., Palin, Searle, et al., 2014; Palin, St-Onge, et al., 2014). The rest of the post-peak assemblage is typical of an amphibolite facies retrograde assemblage characterized by fine-grained amphibole and plagioclase intergrowths. Aggregates of chlorite and biotite characterize a lower amphibolite facies overprint. Rutile is found within prograde relict garnets as well as the matrix and has no indication of internal zonation. We therefore interpret rutile as a relict grains from a prograde or peak assemblage, rather than a new phase that nucleated during latest-stage lower amphibolite facies metamorphism. Zircon is present throughout this sample, predominantly as inclusions in peak omphacite and quartz, suggesting that it crystallized at eclogite-facies conditions.

3.3.4. Correlation of Metamorphic Assemblages (M1, M2, M3) in the Puga Gneiss and Mafic Eclogites

Comparison and correlation of the petrography and petrology of samples 05-02, a03-16, and a03-12, allows for the definition of three distinct metamorphic assemblages that reflect distinct portions of the same P-T path of the Tso Morari complex, experienced and recorded by both lithologies. These assemblages are correlated with the stages defined by St-Onge et al. (2013) (M1, M2, M3). Crucially, these assemblages provide a robust means for linking accessory phase geochronology to metamorphic evolution of the Tso Morari complex. These metamorphic assemblages and their constituent accessory phases are summarized as follows.

3.3.4.1. M1: Prograde-To-Peak Eclogite Facies Assemblage

Zones P1 and P2 of garnet within the Puga gneiss sample 05-02 and zone E1 and E2 of garnet in the mafic eclogite a03-16 define the M1 prograde-to-peak, eclogite facies assemblage. This includes inclusions of kyanite, quartz, white mica, zircon and rutile, within garnet in Puga Gneiss sample 05-02.

3.3.4.2. M2: Peak Eclogite Facies Assemblage

High-Mg rims of garnet (zones P3 and E3), plus omphacite, phengite, quartz and talc in mafic eclogite sample a03-16 define the M2 peak eclogite facies assemblage. M2 also includes the high-Mg garnet rims in Puga gneiss sample 05-02. Elsewhere in Tso Morari, similar garnet rim compositions in mafic eclogites contain inclusions of coesite or polycrystalline inclusions after coesite (Bidgood et al., 2021; Sachan et al., 2004). Remnants of this assemblage are also preserved by relict garnet in the retrogressed mafic eclogite sample a03-12.

3.3.4.3. M3a/M3b/M3c: Post-Peak Assemblage

The M3 post-peak assemblage reflects continuing metamorphism from eclogite to lower amphibolite facies conditions, and is subdivided to reflect this. In the mafic eclogite samples (a03-16, a03-12), M3a is recorded by growth of coarse-grained blue-green amphiboles in the eclogite facies, which elsewhere in the Tso Morari Complex, has been linked to the breakdown of talc and the influx of fluid at 23 and 19 kbar respectively (Palin, Searle, et al., 2014; Palin, St-Onge, et al., 2014). Post-peak assemblage M3b corresponds to upper amphibolite facies retrograde metamorphism. In the mafic eclogite samples (a03-16, a03-12) M3b is defined by symplectites of fine-grained amphibole and plagioclase intergrowths after omphacite. The lower-temperature association of chlorite with biotite, largely as a replacement of garnet cores in a03-12, is assigned to M3c.

In Puga gneiss sample 05-02, initial garnet breakdown and the associated nucleation of xenotime, occurred at eclogite to upper amphibolite facies, and therefore correlates with either the M3a or M3b post-peak assemblages observed in the mafic eclogites. M3b is defined by the matrix assemblage of quartz + albite + muscovite, which also contains zircon and rutile, and displays quartz microstructures indicating post-peak deformation temperatures of >530°C. M3c corresponds to lower amphibolite facies retrograde metamorphism and is represented by overprinting aggregates of chlorite and biotite after garnet.

4. U-Pb Geochronology

4.1. Analytical Methods

Zircon grains from the heavy, non-magnetic fraction of sample a03-12 were imaged via cathodoluminescence (CL) using an FEI Quanta 650 environmental scanning electron microscope (E-SEM) at the University of Oxford, using a 10 kV electron beam, 16 mm working distance and a beam current of 0.49 nA. Zircon grains from sample 05-02 were also mounted on sticky tape in order to analyze the <10 μm thick rims. Rutile grains chosen for analysis were picked from the non-magnetic fraction and were imaged via backscatter electron imaging (using the same E-SEM) to determine the homogeneity of the grains chosen for analysis. None of the rutile grains showed any evidence of zoning. Xenotime was measured in a polished thin section in order to preserve the petrographic relationships observed.

All geochronology and mineral separation were conducted at the Geochronology and Tracers Facility, British Geological Survey, Nottingham, UK. Laser ablation inductively coupled plasma mass spectrometry (LA-ICP-MS) was conducted using a Nu Instruments AttoM sector-field single-collector ICP-MS, coupled to an Elemental Scientific Lasers 193 nm UC Excimer laser ablation system fitted with a TV2 cell. The method follows that described in Roberts et al. (2016), with uncertainty propagation following recommendations of Horstwood et al. (2016), and age calculation and plotting using IsoplotR (Vermeesch, 2018). Common lead corrected ages, where quoted, use a [207]Pb-based method (Chew et al., 2014) and assume a Stacey and Kramers (1975) initial lead composition, and concordance of the final age. All uncertainties are quoted and plotted at 2σ. LA-ICP-MS dates are quoted with propagation of systematic uncertainties, including reference material and decay constant uncertainties; age uncertainties are also expanded to account for the MSWD where the data exhibit overdispersion (Vermeesch, 2018). Accuracy based on zircon and rutile validation materials was better than 1% for zircon and xenotime and 5% for rutile (Plešovice = 339.1 ± 1.9 Ma; GJ-1 = 596.8 ± 2.9 Ma; Manangotry = 555.48 ± 4.23; R19 = 465.9 ± 3.9 Na; Sugluk = 1,714 ± 30 Ma; and PCA = 1,859 ± 25 Ma). Trace elements were measured

using the same instrumentation as for U-Th-Pb, with the Attom measuring in linkscan mode (see Supporting Information S1 for full analytical protocol), with normalization to GJ-1 zircon (Piazolo et al., 2017) except Ti which used Szymanowski et al. (2018).

Zircon in one sample (a03-12) was further analyzed by CA-ID-TIMS, following analytical and data reduction methods described by Tapster et al. (2016), and utilizing the ET535 EARTHTIME mixed tracer (Condon et al., 2015). The CA-ID-TIMS uncertainties are quoted as analytical only/analytical + tracer-calibration/ analytical + tracer-calibration + decay-constant uncertainty, as per community protocols. Our U-Pb dates can be compared using the intermediate uncertainty, but for the sake of simplicity, we quote the final uncertainty within the discussion such that our dates can be compared with constraints from other absolute and relative chronometry.

4.2. Puga Gneiss (Sample 05-02)

4.2.1. Zircon

Zircon grains in the Puga gneiss sample 05-02 show oscillatory zoning and a euhedral shape, indicative of igneous zircon, with a Th/U of 0.05–0.26. Thin, bright rims (<20 μm) are present surrounding the dark cores. From the epoxy mounted zircon, 33 LA-ICP-MS analyses of zircon cores were obtained from 21 grains. Five ages ranging from 2,481 to 1,020 Ma ($^{207}Pb/^{206}Pb$ age), indicate a population of xenocrystic zircon inherited during emplacement of the Puga gneiss igneous protolith. Nine analyses had ages that were discordant by >10%, and were discarded from age calculation. Of the remaining 19 concordant analyses, 17 spots provide a concordia age of 482 ± 5.9 Ma with a mean square of weighted deviates (MSWD) value of 1.5 (Figure 6a). Using spot analysis of tape-mounted zircon, whereby the outer rim can be targeted more confidently, 64 grains yielded a spread of ages from ca. 569 to 48 Ma (Figure 6b). A broad plateau of ages overlaps the mounted zircon at ca. 480 Ma, consistent with our weighted mean concordia age. The youngest three analyses provide a weighted mean, using common lead corrected $^{206}Pb/^{238}U$ ages, of 48.9 ± 1.2 Ma (MSWD = 1.3; Figure 6b).

4.2.2. Xenotime

Rare 30–100 μm xenotime grains were observed in micaceous aggregates at corroded margins of garnet in sample 05-02, as described above (Figure 3a). The grains show homogenous brightness in BSE indicating the absence of internal zonation. Nine spots were analyzed across 9 grains, and yield a mixing line between radiogenic and common lead components. Using a free regression, the lower intercept age is calculated at 47.4 ± 1.4 Ma (MSWD = 1.9; Figure 6c).

4.2.3. Rutile

Rutile grains in sample 05-02 measure 50–100 μm in size and show homogenous brightness in BSE, indicating the absence of internal zonation. Fourteen spots were analyzed across 14 rutile grains, and yield a mixing line between radiogenic and common lead components. Using a free regression yields a lower intercept age of 40.4 ± 1.7 Ma (MSWD = 2; Figure 6d).

4.3. Retrogressed Mafic Eclogite (Sample a03-12)

4.3.1. Zircon

Zircon grains are rarely found in mafic eclogites of the Tso Morari Complex. In thin section, zircons are often found as inclusions within eclogite-facies phases such as quartz and omphacite. Separated zircon grains from sample a03-12 are translucent and colorless with rounded and euhedral grain shapes and a grain size of <70 μm (Figure 7f). They have zoning patterns dominated by broad oscillatory or sector zoning, that in some grains, truncates a darker core region; the latter were not analyzed.

Thirteen laser spot analyses were performed on the cores of 13 zircon grains separated from sample a03-12 for U-Pb, with 3 analyses rejected due to Pb counts below detection. The U concentrations are variable (13.5–1,528 ppm), and the degree of discordance varies between 0.1% and 12%. Of the remaining 10 analyses, the lower intercept of 9 spots is calculated using a free regression at 47.5 ± 1.7 Ma (MSWD = 0.63; Figure 7a). These zircon analyses have low Th/U ratios (<0.01). The result implies that the data conform to a single population. The
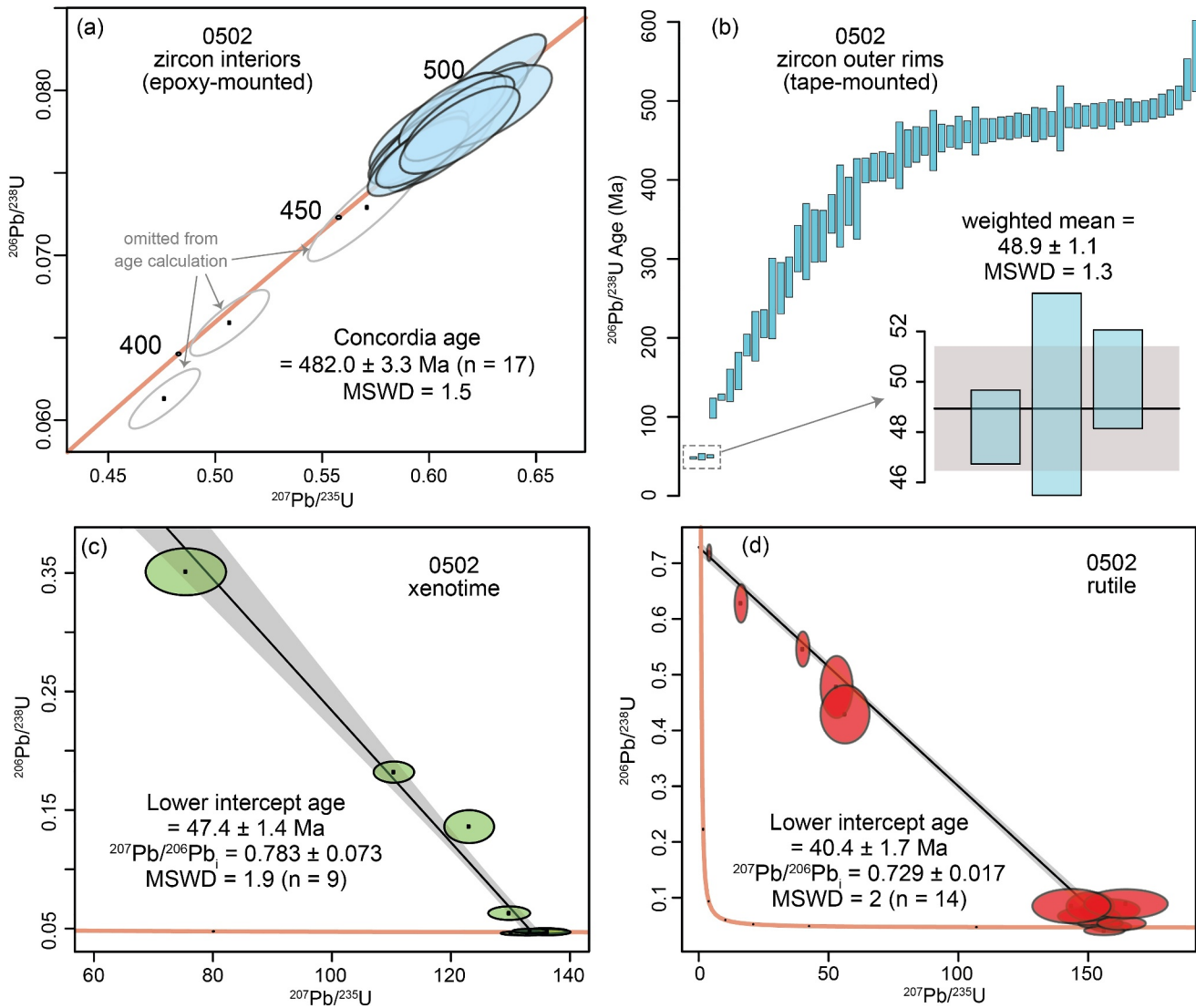
Figure 6. (a) U-Pb Wetherill plot showing U-Pb zircon core analyses of Puga Gneiss sample 05-02. (b) Rank-plot of all $^{206}Pb/^{238}U$ zircon date s. An older age plateau represents the zircon cores at ~480 Ma. The youngest dates represent thin rims, and converge on a Himalayan age with a weighted average $^{206}Pb/^{238}U$ age of the three youngest zircon dates. (c) Tera-Wasserburg plot of xenotime U-Pb analyses. (d) Tera-Wasserburg plot of rutile U-Pb analyses. Box heights and uncertainty ellipses are 2σ uncertainties.

omitted analysis has a much higher Th/U ratio (0.25), suggesting an igneous core region was clipped during the ablation.

Trace elements were measured on 20 zircon grains, including adjacent spots on the same 13 grains analyzed for U-Pb; 3 analyses were omitted due to inclusions. Ti-in-zircon temperatures are calculated using Si and Ti activities of 1.0, and the equation of Ferry and Watson (2007). The temperatures range from 603 to 724°C, forming a normal distribution around a peak at ca. 630°C (Figure 7c). The REE data are plotted as chondrite-normalized values (Figure 7d). The REE patterns of zircon are broadly consistent across multiple grains, with no Eu anomaly, flat HREE patterns and depleted LREEs.

Several zircon grains were extracted from the resin mounts and prepared as single grain aliquots for CA-ID-TIMS. The resulting data are six reproducible fractions yielding a weighted mean (Th-corrected) $^{206}Pb/^{238}U$ age of 46.912 ± 0.068 Ma with an MSWD of 0.2 (Figure 7b).
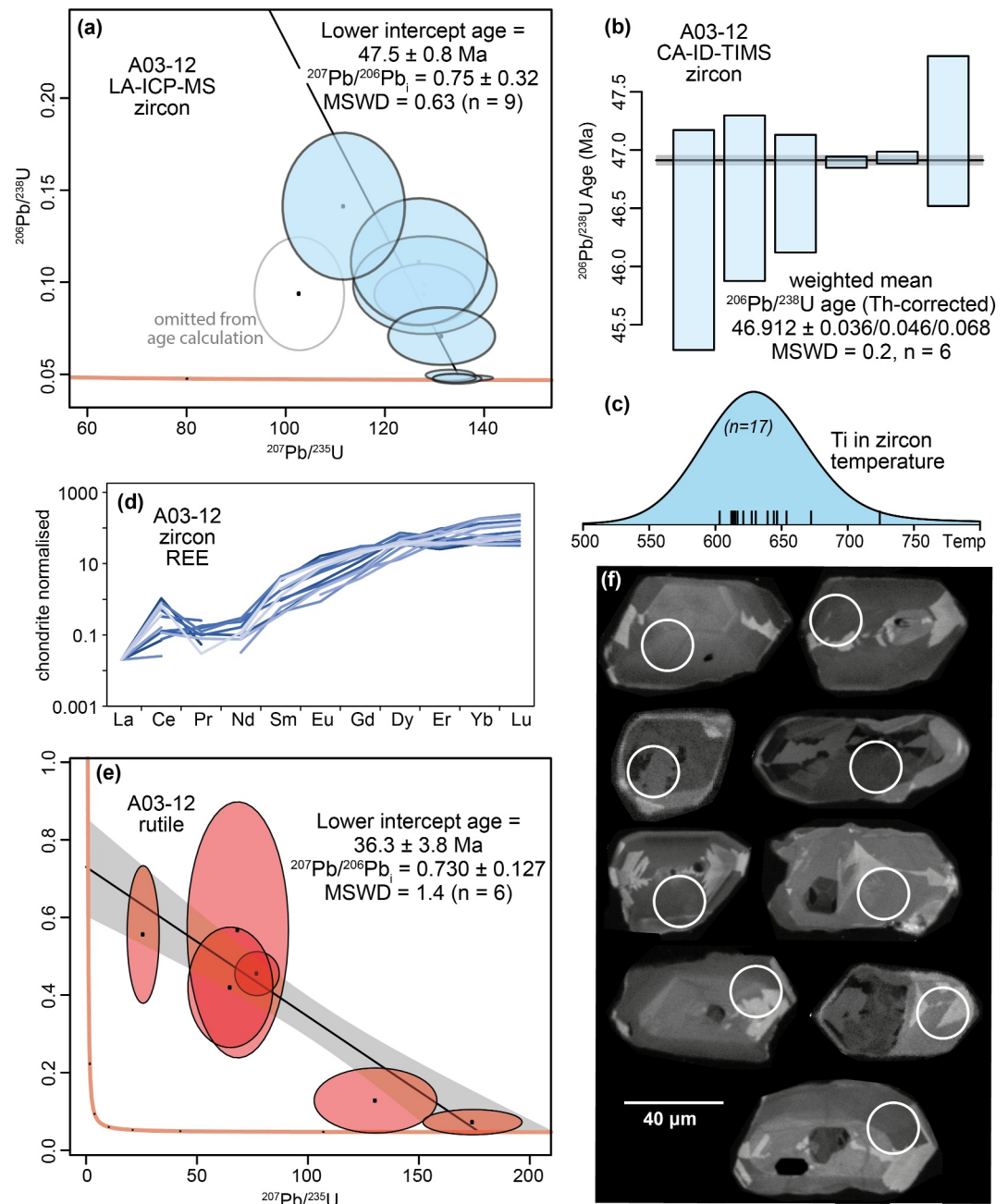
Figure 7. Mafic eclogite sample a03-12 (a) Tera-Wasserburg plot of LA-ICP-MS U-Pb data for zircon, with lower intercept $^{206}Pb/^{238}U$ age. (b) Weighted mean $^{206}Pb/^{238}U$ (Th corrected) age of 6 zircon grains using CA-ID-TIMS. uncertainties are quoted as analytical only/analytical + tracer-calibration/analytical + tracer-calibration + decay-constant uncertainty. (c) Histogram of Ti in zircon temperatures. (d) Sample a03-12 zircon chondrite-normalized REE data. (e) Tera-Wasserburg plot of LA-ICP-MS U-Pb data for rutile, with lower intercept $^{206}Pb/^{238}U$ age. (f) Cathodoluminescence images of zircon separates from sample a03-12. All box heights and uncertainty ellipses are 2σ uncertainties.

4.3.2. Rutile

Rutile grains in sample a03-12 show homogenous brightness in BSE with no indication of internal zonation. The majority of analyses had Pb counts below detection, the remaining data comprise six spots analyzed across 6 grains. The analyses are distributed between the radiogenic and common lead components, and using a free regression, yield a lower intercept age of 36.3 ± 3.8 (MSWD = 1.4; Figure 7e).
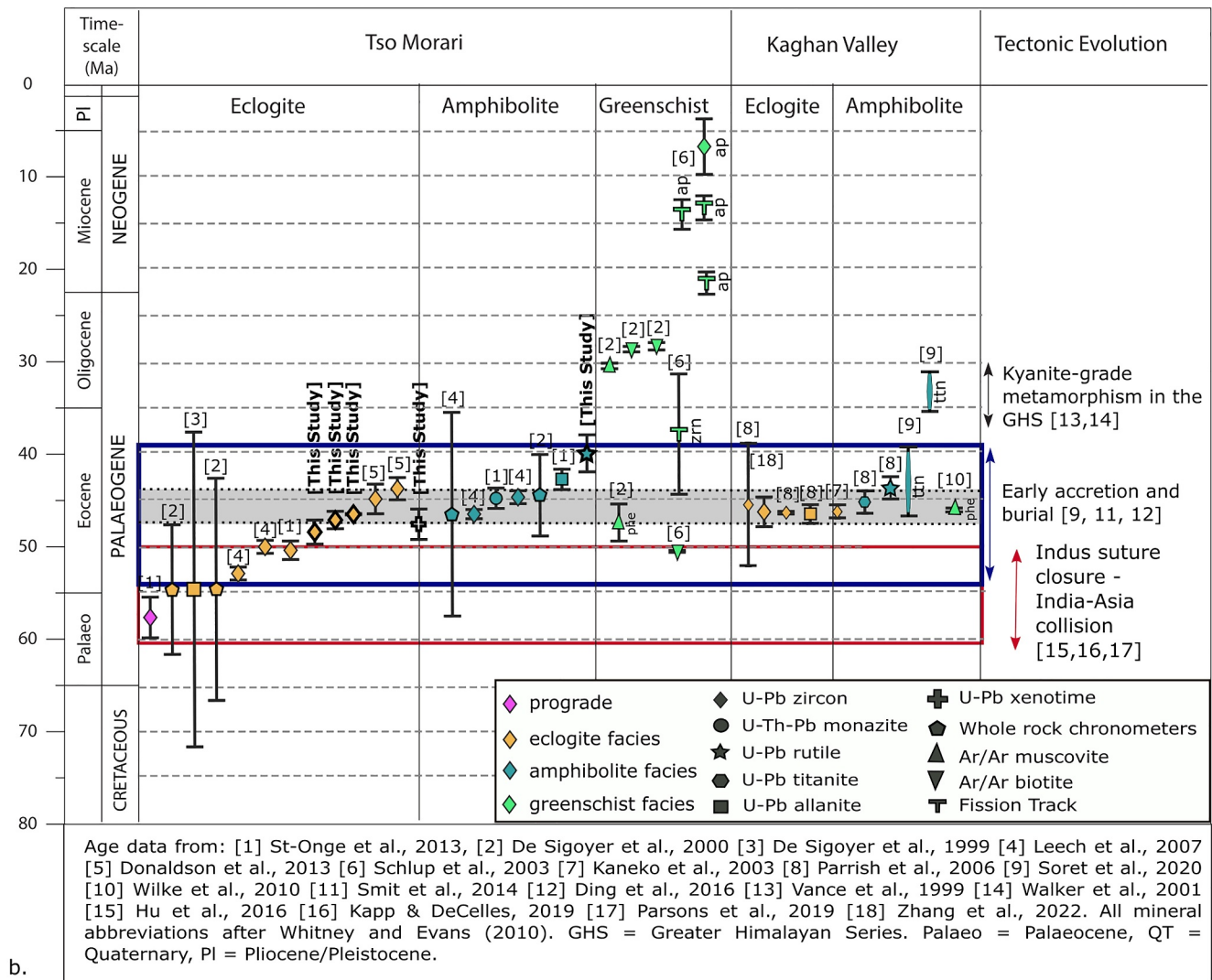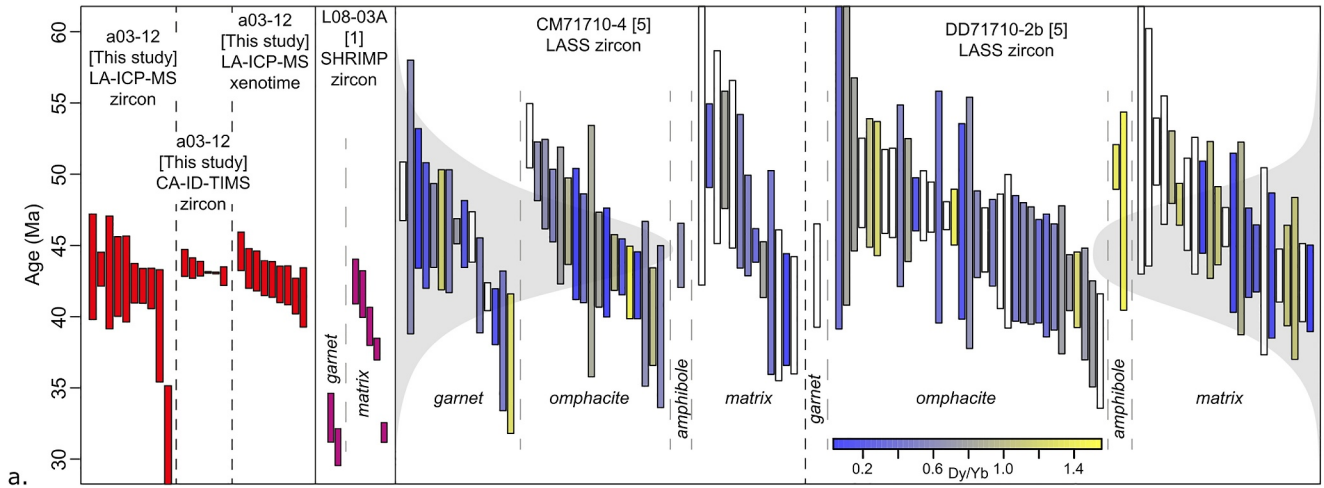
Figure 8. (a) Zircon data for individual samples from this study, St-Onge et al. (2013) and Donaldson et al. (2013). Blue-yellow color scale represents Dy/Yb. Solid colors do not contain individual REE spot data. Sample histograms shown in gray for Donaldson et al. (2013). (b) Time chart for Tso Morari and Kaghan, after (Palin et al., 2012), comprising data from multiple sources, including this study.

4.4. Summary and Interpretations

4.4.1. Puga Gneiss (Sample 05-02)

Zircon core ages of 482.0 ± 5.9 Ma in the Puga Gneiss are interpreted to represent the igneous crystallization age and are comparable with U-Pb zircon ages of 479 ± 1 Ma in both the Polokongka La granite and the Puga Gneiss (Girard & Bussy, 1999). A monazite age of 473 ± 9 Ma in the Polokongka La granite, interpreted to have formed during crystallization of the granite (Bidgood et al., 2023), also overlaps with the age of zircon crystallization. Rim analyses of Ordovician zircon from the Puga Gneiss yielded an age of 48.9 ± 1.2 Ma (LA-ICP-MS), which overlap with high precision CA-ID-TIMS zircon age from mafic eclogite a03-12 (hosted within the gneiss), suggesting that zircon rims in the Puga gneiss also grew at eclogite-facies conditions.

Xenotime is found exclusively in Puga Gneiss sample 05-02, in mica aggregates adjacent to the corroded outer rim of a large garnet porphyroblast (Figures 2 and 3). Breakdown of parts of the Mg-enriched garnet rims, formed under peak eclogite-facies conditions (M2), liberated Y, which is concentrated in garnet zones P2 and P3 (Figure 3a), for xenotime growth. We therefore interpret the U-Pb xenotime age in sample 05-02 (47.4 ± 1.4 Ma) as the age of initial garnet breakdown during decompression. The xenotime age overlaps with the eclogite facies zircon rim age within the same sample 05-02 (48.9 ± 1.2 Ma), as well as the precise eclogite-facies zircon CA-ID-TIMS age of mafic eclogite sample a03-12 (46.912 ± 0.068 Ma), located within the same structural unit. This allows us to assign the xenotime crystallization and garnet breakdown in the Puga Gneiss sample to the M3a metamorphic assemblage, reflecting the earliest phase of decompression at eclogite facies conditions.

Rutile is present as inclusions within prograde (M1) to peak pressure (M2) garnets and the matrix of the Puga Gneiss. Given that the peak temperature of the Tso Morari Complex (705–755°C, St-Onge et al., 2013) is greater than the closure temperature of rutile at ~400–630°C (Cherniak, 2000; Kooijman et al., 2010; Mezger et al., 1989; Vry & Baker, 2006), which is dependent on cooling rate and grain size (Oriolo et al., 2018; Zack & Kooijman, 2017), the U-Pb age of rutile can therefore be attributed to cooling of the Puga Gneiss through the rutile closure temperature at 40.4 ± 1.1 Ma, after peak temperature conditions.

4.4.2. Retrogressed Mafic Eclogite (Sample a03-12)

LA-ICP-MS analyses of zircon from mafic eclogite sample a03-12 are entirely <50 Ma, and provide a weighted mean age of 47.5 ± 1.7 Ma. Although a limited data set (9 analyses), our result implies a single population of metamorphic zircon, rather than preserving a protracted history of zircon growth. Flat HREE profiles and the lack of an Eu anomaly in the core and mantle of zircon grains are indicative of crystallization in garnet-present, plagioclase-absent conditions, consistent with crystallization in the eclogite facies (Rubatto, 2002; Rubatto & Hermann, 2003; Schaltegger et al., 1999). The measured zircon date is therefore interpreted to correspond to growth within the eclogite-facies. Ti in zircon temperatures of 603–724°C lie below the closer temperature of Ti in zircon (~900°C, Cherniak et al., 2007; Watson et al., 2006) and is therefore interpreted as the zircon crystallization temperature.

The zircon CA-ID-TIMS data from mafic eclogite sample a03-12 are tightly clustered yielding a date of 46.91 ± 0.068 Ma, which we interpret as the age of zircon growth at eclogite facies conditions (M1-3a). We note that this interpretation is heavily weighted to only the two analyses of the most U-rich zircon, excluding these analyses yields a weighted mean of 46.71 ± 0.33/0.38/0.38 Ma (MSWD = 1.04; n = 4) and is therefore within uncertainty of the original interpretation. Regardless of interpretation, the uncertainty associated with the CA-ID-TIMS data is 1–2 orders of magnitude smaller than LA-ICPMS U-Pb data and provides the most precise estimate of the timing of metamorphic zircon growth from Tso Morari thus far. Additionally, even with the improved precision, the analyses and the lack of dispersion indicated by their MSWDs suggests no measurable crystal to crystal variation at around the ~1 Myr resolution.

Rutile is the peak titanium-bearing phase in mafic rocks during eclogite-facies metamorphism and is present as inclusions in garnet (M1), as well as in the matrix (M2-3b). Peak temperature in the Tso Morari Complex is estimated at 600–755°C (De Sigoyer et al., 2000; St-Onge et al., 2013), above the predicted closure temperature of rutile at ~400–630°C (Cherniak, 2000; Kooijman et al., 2010; Mezger et al., 1989; Vry & Baker, 2006) which is dependent on cooling rate and grain size (Oriolo et al., 2018; Zack & Kooijman, 2017). The U-Pb age of rutile can therefore be attributed to cooling through this closure temperature range.

5. Metamorphism, Deformation and Geochronology of the Tso Morari Complex

Previous studies indicate that subduction, exhumation and emplacement of the Tso Morari Complex took place between c. 60 Ma and c. 7.5 Ma (Figure 6), with exhumation to lower crustal conditions by 45.3 ± 1.1 Ma at an average rate of ~12 mm a^{-1} (St-Onge et al., 2013). The texture and composition of the mafic eclogites and Puga gneiss samples in this study collectively provide a record of initial exhumation from UHP eclogite-facies conditions, followed by exhumation through crustal conditions. Integrating this information with our new high-precision geochronology from a range of accessory phases which crystallized at different stages of metamorphism allows us to constrain the timing of mineral growth and fabric development with respect to the burial and exhumation of the Tso Morari Complex.

Evidence of prograde metamorphism to peak pressures (M1-2) is preserved within garnets from mafic eclogite and the Puga Gneiss, comparable to that observed in the eclogite studied by St-Onge et al. (2013). The garnet-bearing Puga Gneiss, as represented by sample 05-02, is not typical of the host Puga Gneiss, which generally preserves only amphibolite-facies assemblages. The formation and preservation of garnet in this sample is therefore particularly valuable given that it records the same overall prograde compositional trends as seen in the Tso Morari eclogites. The analyzed garnet (Figures 3a and 3b) also contains complex deformation fabrics and inclusion suites, indicating that deformation and transformation of the original granite was already underway prior to garnet growth (M1) in at least part of the complex. Early fabrics are rarely preserved in the Tso Morari Complex, where the earliest stage of macroscopic deformation has been previously identified as the dominant top-to-the-east exhumation fabric within the Puga Gneiss, and is attributed to initial M3a exhumation from eclogite-facies conditions (Epard & Steck, 2008).

Our eclogite-facies zircon dates of 46.912 ± 0.068 Ma (CA-ID-TIMS) and 47.5 ± 1.7 Ma (LA-ICPMS) from a mafic eclogite overlap with our zircon rim and xenotime dates in the Puga Gneiss. We interpret this overlap as a record of the earliest phase of decompression at 630°C and eclogite facies conditions, as recorded by the Ti in zircon temperatures and the partial breakdown of yttrium-bearing garnet rims. The crucial breakdown of the garnet rim zones and fracture-based alteration, with xenotime among its products, provides insight into the early exhumation history of these rocks that is not recorded elsewhere, but predates the Barrovian overprint of 7.0–8.4 kbar, 705–755°C recorded at 45.3 ± 1.1 and 43.3 ± 1.1 Ma by St-Onge et al. (2013).

The formation of quartz microstructures during high-temperature (>530°C) dynamic recrystallization indicates that deformation took place during exhumation to crustal conditions (M3b). There is no significant later overprinting of quartz deformation fabrics in Puga Gneiss samples from the core of the dome (Bidgood, 2020), implying a lack of pervasive deformation below 530°C. Deformation therefore occurred prior to cooling through the rutile closure temperature of ~630–400°C (Cherniak, 2000; Li et al., 2013; Mezger et al., 1989; Vry & Baker, 2006) at 40.4 ± 1.1 Ma and was ductile and pervasive. This interpretation is confirmed by Dutta and Mukherjee (2021) who predict deformation temperatures >600°C based on misorientation analysis and micro-textural evidences of incipient partial melting in the Puga gneiss. Subsequent deformation during exhumation relating to doming and emplacement (M3c) was not pervasive, with foliations and lineations developing at the margins of the dome, adjacent to the normal sense shear zones (e.g., Zildat-Ribil fault, Bidgood, 2020; Dutta & Mukherjee, 2021; Epard & Steck, 2008). The age of exhumation of the Tso Morari dome is recorded by the Ar-Ar muscovite and biotite and apatite fission track dates of <32.4 Ma (De Sigoyer et al., 2000; Schlup & Carter, 2003) which record cooling through the Ar closure temperatures of muscovite (~425°C, Harrison et al., 2009), biotite (<345°C, Harrison et al., 1985) and apatite (<135°C, Warnock et al., 1997) respectively.

6. Discussion

6.1. Continental Subduction and Exhumation in the NW Himalaya

Our petrographic correlation of zircon and xenotime ages with the M3a assemblage indicates that zircon growth at ~47–46 Ma took place at subsolidus conditions during the earliest stages of decompression from UHP conditions. These ages overlap with the zircon age distribution peak of 47–43 Ma recorded by Donaldson et al. (2013). Considering their analytical scatter (i.e., MSWDs of 2.4 and 3.4) the Donaldson et al. dates have reasonable agreement with our 47–46 Ma age, however, those data were previously interpreted as a record of UHP

metamorphism, starting at ~47 Ma. It is therefore necessary to reassess the Donaldson et al. (2013) data in light of our new data and observations, as follows.

Subsolidus zircon growth requires a fluid phase to mediate the liberation of Zr from Zr-bearing phases (ilm, ru, cpx, grt) (Chen & Zheng, 2017; Chen et al., 2010; Kohn et al., 2015; Skuzovatov et al., 2021). The host rock in the Tso Morari complex is a dry granite with intruded mafic dykes (see Bidgood et al., 2023) resulting in restricted opportunity for prograde/peak zircon growth. Palin, Searle, et al. (2014) and Palin, St-Onge, et al. (2014) determined that the first pulse of post-peak fluid in the eclogite facies relates to the destabilization of talc and growth of the coarse-grained amphiboles at ~23 kbar, followed by fluid infiltration from an external source at ~19 kbar. Coarse-grained, zoned amphiboles are abundant in mafic eclogites from across the Tso Morari Complex suggesting that post-peak eclogite facies hydration was a common and widespread occurrence, aided further by exhumation-related deformation. These influxes of fluid during exhumation, subsequent to a potentially dry spell at prograde to peak conditions, would have provided conditions favorable for high concentrations of zircon growth. Consequently, we argue that the breakdown of UHP garnet rims recorded by xenotime at 47.4 ± 1.4 Ma indicates that the zircon age peak at 47–43 Ma of Donaldson et al. (2013), along with our own CA-ID-TIMS zircon age of 46.91 ± 0.068 Ma, reflects a pulse of zircon growth during the onset of exhumation from UHP conditions, aided by the exhumation-driven liberation of fluids.

Based on the above conclusion, older dates in previous studies, including a 58 ± 2.2 Ma (n = 2) zircon age from St-Onge et al. (2013) and apparent older zircon dates (55–48 Ma) from Donaldson et al. (2013), may record zircon growth during prograde to peak metamorphism. However, it is difficult to place them in a robust context given: (a) the proportion of common lead for most of the analyses; (b) the potential ablation of older zircon domains reflecting the protolith age; and (c) the lack of relationship between textural location and REE chemistry (Figure 8a). The nature of apparent younger common-lead corrected dates from the Donaldson et al. (2013) data set also remain uncertain for the same reasons; younger dates could plausibly record continued zircon growth during decompression, but dates younger than the ca. 40 Ma rutile age imply these may relate to analytical inaccuracies. Given that we consider our xenotime date as a marker for the onset of UHP exhumation, we suggest that the Donaldson et al. (2013) data reflect zircon growth due to fluid infiltration at and after 47 Ma.

Our new CA-ID-TIMS zircon age of 46.912 ± 0.068 Ma more closely and precisely correlates with ages from zircon (46.4 ± 0.1 Ma—ID-TIMS; 46.2 ± 0.7—SHRIMP, 46 ± 2 Ma—SIMS) and allanite (46.5 ± 1.0 Ma—ID-TIMS) in UHP assemblages from Kaghan, located 450 km to the west of Tso Morari (Kaneko et al., 2003; Parrish et al., 2006; Zhang et al., 2022) (see Figure 8). We do not think this is coincidental; metamorphic P-T data from both of these units record similar prograde (up to UHP metamorphism) and retrograde (including UHP exhumation and exhumation through the crust) P-T paths. In Kaghan, coesite is found in thin metamorphic zircon rims in the felsic gneiss, indicating that zircon crystallization occurred at UHP conditions (Kaneko et al., 2003). In the Tso Morari Complex, coesite is observed in the outermost rims of prograde garnets but has not yet been observed as inclusions in zircon. Quartz microstructures after the presence of former coesite are also reported from the Polokongka La Granite of the Tso Morari Complex (Bidgood et al., 2021). Based on these similarities, we argue that the overlap in ages between Tso Morari and Kaghan indicates that UHP exhumation and associated fluid flux at 47–46 Ma was responsible for a ubiquitous pulse of zircon growth across the NW Himalaya, occurring at the same time as or shortly after the achievement of maximum P and T under UHP conditions. We suggest that the regional synchroneity between Tso Morari and Kaghan, across a distance of ~450 km, reflects the scale at which slab dynamics control metamorphism and exhumation with a subduction zone setting.

The mode of UHP exhumation is unclear from our data. Isothermal, triclinic deformation during exhumation of the Tso Morari complex, as reported by Long et al. (2020) and Dutta and Mukherjee (2021), is most compatible with the recirculation model and plunger model of Warren et al. (2008a, 2008b, 2008c). These models invoke the transport of crustal slices of the lower plate from UHP pressures along the subduction interface, rather than wholesale exhumation of the subducting slab, and can therefore occur independently from, and without need for slab break-off. The timing of slab break-off cannot be resolved from our data and therefore remains debated, with estimates ranging widely between ~50 and 10 Ma (see reviewed compilation of Garzanti et al., 2018).

Lastly, cooling through the rutile closure temperature took place ~3.7 Ma later in Tso Morari than Kaghan (see Figure 8). At face value, this implies a longer period of time between zircon growth and exhumation through the rutile closure temperature for the Tso Morari Complex, relative to Kaghan. However, uncertainties in the exact

conditions of zircon growth and rutile closure temperature prevents us from making any meaningful interpretation for the cause of this difference.

6.2. Geodynamic Significance of UHP Exhumation During the Himalayan Orogeny

Our data suggest that zircon crystallization recorded in the Tso Morari complex and Kaghan at 47–46 Ma, corresponds to the onset of exhumation of Indian continental crust from UHP conditions. In the following sections, we consider the geodynamic significance of this event with respect to the wider metamorphic, magmatic and plate kinematic evolution of the Himalayan orogeny and the India-Australia-Eurasia plate network (Figures 9 and 10).

6.2.1. UHP Exhumation During the Himalayan Orogeny

When placed in context with the bedrock record of collision, our constraints for the onset of UHP exhumation in the NW Himalayan reveal how changes in subduction dynamics affected the structural, magmatic, and metamorphic evolution of the Himalayan orogeny (Figure 9).

In the lower plate (Indian crust), the onset of UHP exhumation at 47–46 Ma overlaps with the onset of local prograde amphibolite facies, Barrovian-style metamorphism in the NW Himalaya at 47–39 Ma (Soret et al., 2021) (Figure 9a). This was followed by wide-spread amphibolite facies metamorphism of the Himalayan metamorphic core (HMC) across the rest of the Himalaya during crustal thickening of the HMC from ~41 Ma through to ~17 Ma (Figure 9a) (Ambrose et al., 2015; Carosi et al., 2016, 2019; Goscombe et al., 2018; Ji et al., 2024; Mottram et al., 2019; Waters, 2019), whilst high-pressure eclogite to granulite facies metamorphism of Indian lower crust is recorded in localized occurrences across the orogen from 40 to 25 Ma (Figure 9a) (Chen et al., 2022; O'Brien, 2019a).

UHP exhumation at 47–46 Ma also overlaps with significant magmatic and metamorphic changes in the upper plate of the orogen (Eurasian crust) (Figure 9a; see also Figure 10c for locations). Between 50 and 40 Ma, isotopic signatures of magmatic rocks from the Kohistan-Ladakh batholith record increased crustal contamination of arc magmatism (Figure 9a) (Bouilhol et al., 2013; Jagoutz et al., 2019). Along the Lhasa block, the Gangdese arc records adakite magmatism from ~48 Ma produced by melting of the Tibetan lower crust (e.g., Guan et al., 2012; Ma et al., 2014; Searle et al., 2011), and the cessation of subduction-related magmatism by ~40 Ma (Figure 9a) (e.g., Zhu et al., 2019). At the same time, the Lhasa block recorded high pressure-low temperature kyanite-grade partial melting associated with deformation and crustal thickening at 44–32 Ma (Figure 9a) (Palin, Searle, et al., 2014; Palin, St-Onge, et al., 2014; Zhang et al., 2010). Further to the east, the Mogok metamorphic belt and Eastern Ophiolite Belt in Myanmar record sillimanite-grade metamorphism between 48 and 22 Ma, which included a phase of granulite facies metamorphism between 43 and 32 Ma (Figure 9a) (Barley et al., 2003; Lamont et al., 2021; Searle et al., 2007, 2017, 2020).

Collectively the structural, metamorphic, and magmatic changes recorded in both the lower and upper plates of the Himalayan orogeny between ~50 and 40 Ma (Figure 9a) reflect (a) a warming metamorphic thermal gradient (e.g., Chen et al., 2022; Ji et al., 2024; Soret et al., 2021); (b) greater mechanical coupling of the upper and lower plates resulting in increased crustal shortening and thickening; and (c) a greater contribution of Indian continental crustal material to upper plate magmatism. These phenomena are best explained by a reduction in the dip of the subducting Indian plate beneath Eurasia during that time (Figures 10a and 10b) (e.g., Chen et al., 2022; Ji et al., 2024; Soret et al., 2021). We attribute this to the early stages of the India-Asia collision sensu stricto (i.e., second collision of the Himalayan orogeny), whereby the positive buoyancy of the Indian continental crust stalled subduction of the Indian plate beneath the Eurasian margin (Figure 9b).

6.2.2. A Shift in Orogenic Regimes

UHP exhumation at 47–46 Ma marks a significant geodynamic shift in the orogenic regime of the collision zone (Figures 9b, 10a, and 10b). Prior to this time, India-Asia convergence was accommodated by subduction of Indian and/or Neotethys oceanic lithosphere beneath Eurasian. Then, following the India-Asia continent-continent collision sensu stricto by 47 Ma, the reduced dip of the Indian slab increased the mechanical coupling between upper and lower plates and the component of convergence accommodated by crustal shortening. This switch in mode of convergence can be viewed as a shift in the orogenic regime of the collision zone (cf. Cawood
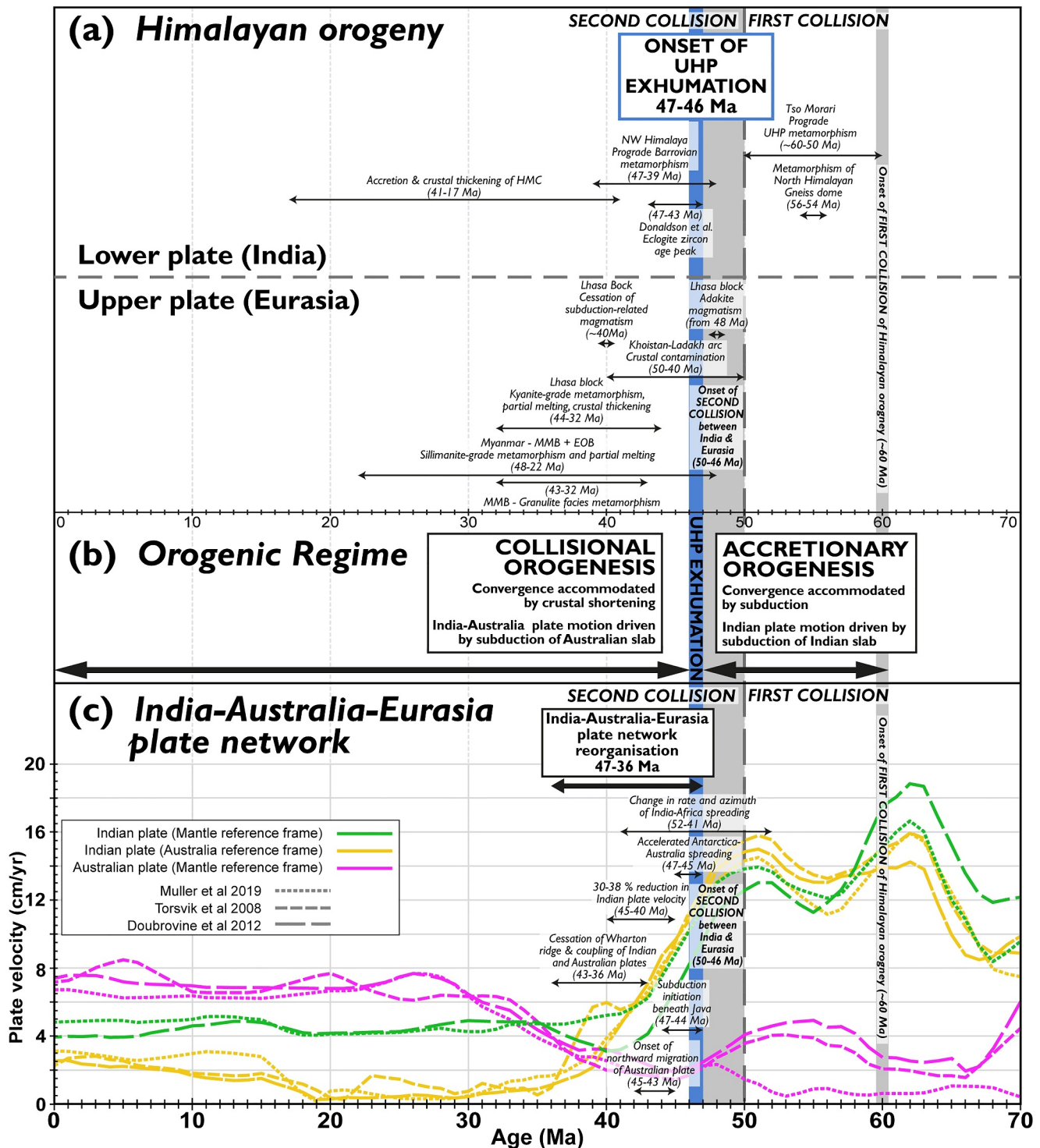
Figure 9. UHP exhumation at 47–46 Ma and its temporal relationship with the metamorphic, magmatic, and plate kinematic evolution of the Himalayan orogeny and India-Australia-Eurasia plate network. (a) Metamorphic and magmatic events in the Himalayan orogeny. (b) Orogenic regime of the Himalayan orogeny: onset of UHP exhumation marks the transition from an accretionary orogen to a collisional orogen (cf., Cawood et al., 2009). (c) Reorganization of the India-Australia-Eurasia plate network at 47–36 Ma with plate velocity profiles for the Indian and Australian plates (Doubrovine et al., 2012; Müller et al., 2019; Torsvik et al., 2008) plotted using GPlates (Müller et al., 2018). Data sources for events in (a) and (c) are cited in the main text. (c) Is modified after Parsons et al. (2021). EOB—Eastern Ophiolite Belt; HMC—Himalayan Metamorphic core; MMB—Mogok Metamorphic Belt.

(a) 50-47 Ma: Onset of India-Asia collision

(b) 47-46 Ma and younger

Gangdese arc (Lhasa block)

India / Asia

UHP metamorphism of Tso Morari

SLAB SCENARIO 1:
UHP is facilitated by
slab break-off at 47-46 Ma

xxxxx

Steep subduction
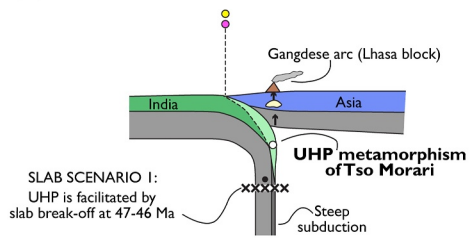
Prior to collision:
Asian active margin = Accretionary Orogen
Convergence accommodated by subduction
Convergence driven by subduction of Indian slab

North migration of collision zone

Crustal thickening & Barrovian metamorphism

Continental contamination of arc magmatism + adakite produced by lower crustal melting

Shallowing of slab dip

xxxxx

UHP exhumation of Tso Morari

SLAB SCENARIO 2 (DASHED LINES):
Slab break-off occurs later (post-40 Ma)
Buoyancy of Indian continent drives UHP
exhumation and results in lateral slab dragging

India-Asia collision zone = Collisional Orogen
Convergence accommodated by crustal shortening
± continental subduction
Convergence driven by subduction of Australian slab
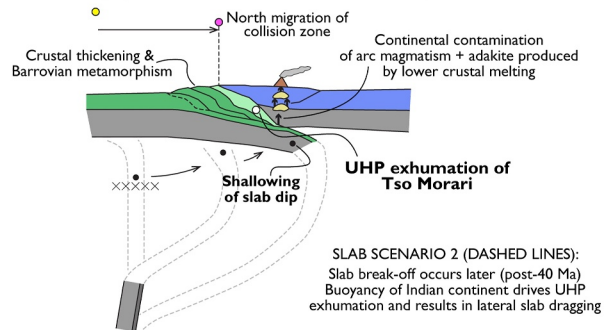
Legend:
- Tso Morari Complex (plus THS ± GHS)
- Indian continental crust (LHS)
- Asian continental crust
- Oceanic crust
- Lithospheric mantle
- Stationary (i.e. mantle) reference point
- Suture zone reference point
- Tso Morari UHP reference point
- Indian slab reference point

(c)

47-46 Ma:
ONSET OF UHP EXHUMATION MARKS CHANGE IN SUBDUCTION DYNAMICS OF INDIA-ASIA COLLISION

46 Ma Reconstruction:
Eocene plate network reorganization
Triggered by changes in subduction dynamics forced by onset of the India-Asia collision

EURASIA

khl / lh / GI / mk / wb

INDIA

45-40 Ma: 30%–38% reduction of IND plate speed

47-44 Ma: Onset of subduction of the AUS plate beneath Java (ja)

ja

41 Ma: Southwestward jump of the Central India ridge (CIR)

AFR

IND

CIR

52-41 Ma: Clockwise rotation and reduction in rate of IND-AFR spreading azimuth

43-36 Ma: Cessation of Wharton Ridge (WR) & coupling of IND & AUS plates

WR

AUS

45-43 Ma: Onset of northward motion of AUS plate

ANT
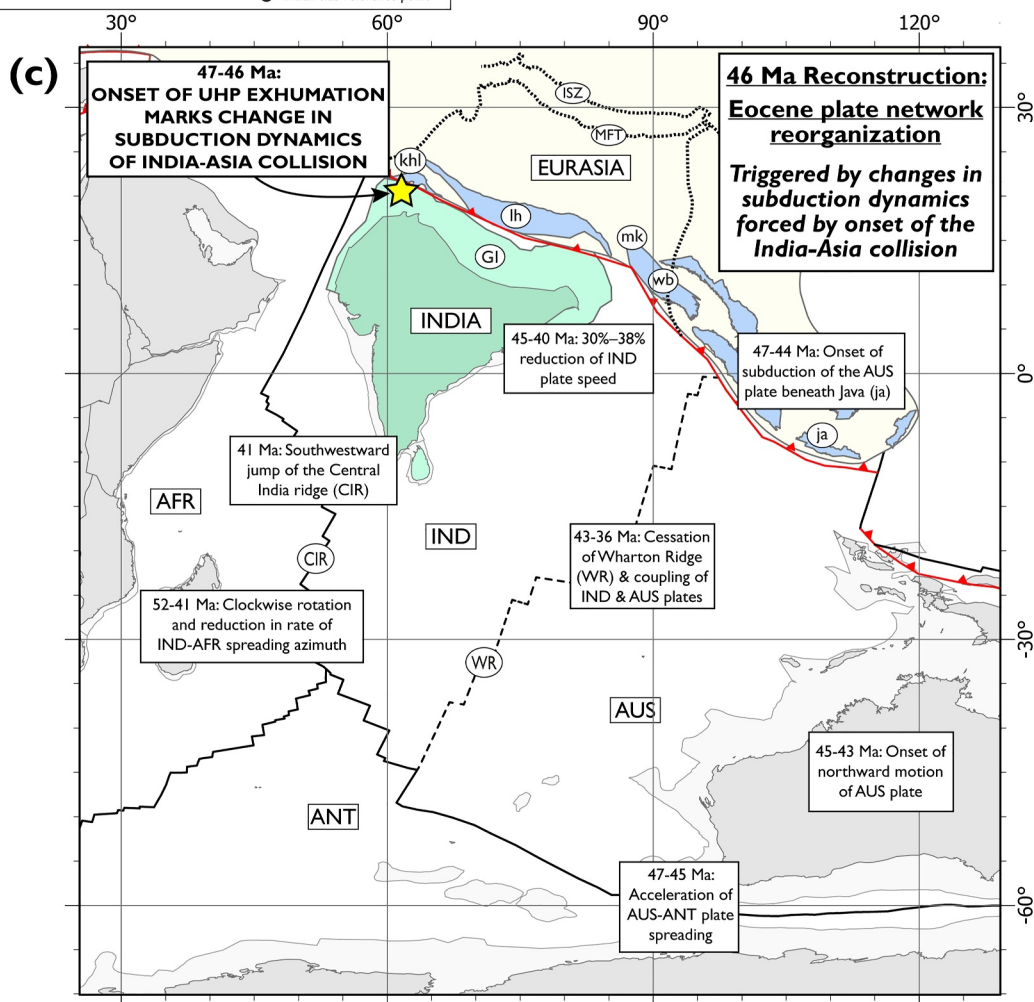
47-45 Ma: Acceleration of AUS-ANT plate spreading

Figure 10.

et al., 2009) from (a) an *accretionary orogen*, in which India-Asia convergence was driven and accommodated by subduction of Indian and/or Neotethys oceanic lithosphere (Figure 10a); to (b) a *collisional orogen*, in which India-Asia convergence was accommodated by crustal shortening (e.g., Chen et al., 2022; Parsons et al., 2021; Replumaz et al., 2014), and driven by northeastward subduction of Indian-Australian oceanic lithosphere beneath SE Asia, further to the east (Figure 10b) (e.g., Bose et al., 2023; Capitanio et al., 2015; Li et al., 2008; Parsons et al., 2021). The onset of UHP exhumation at 47–46 Ma therefore timestamps the change in orogenic regime of the India-Asia collision zone from an *accretionary orogen* to a *collision orogen* (cf. Cawood et al., 2009) (Figure 9b).

6.2.3. Implications for Models of the Himalayan Orogeny and the India-Asia Continent-Continent Collision (Sensu Stricto)

We interpret the onset of the India-Asia collision (sensu stricto) to occur at ∼50–47 Ma, based on (a) our constraint for the onset of UHP exhumation at 47–46 Ma; (b) a reduction in Indian plate velocity starting at ∼50 Ma (Figure 9c); (c) plate reconstructions of the restored Indian and Eurasian margins at 50–45 Ma (Figure 10b) (Parsons et al., 2021; Replumaz et al., 2014); and (d) changes in the magmatic and metamorphic evolution of the Eurasian margin (upper plate) between 50 and 40 Ma (listed above) (Figure 9a).

In the context of our data, single collision models initiating at ∼60 Ma (e.g., Hu et al., 2016; Ingalls et al., 2016) would require ∼14 Myrs of uninterrupted continental subduction prior to UHP exhumation of Tso Morari at 47–46 Ma. This equates to wholesale subduction of a 2,500 × 2,000 km area of Indian continental lithosphere. This scenario remains highly disputed and is not discussed further as it is yet to be shown that such extreme volumes of continental subduction are feasible or sustainable (Afonso & Zlotnik, 2011; Ingalls et al., 2016; Parsons et al., 2020; van Hinsbergen et al., 2019).

In the context of double-collision models for the Himalayan orogeny, prograde to peak metamorphism of the Tso Morari complex between 60 and 50 Ma (Donaldson et al., 2013; Leech et al., 2007; St-Onge et al., 2013), as well as Barrovian metamorphism of the North Himalayan gneiss domes between 56 and 54 Ma (Ding et al., 2016; Smit et al., 2014), may be explained by initial burial of the NW Himalaya during the first collision event of the Himalayan orogeny (Figure 9a) (first collision began at ∼61 Ma, see introduction for definitions). Our new data do not permit us to constrain the validity of the opposing hypotheses for first collision beyond that which is already discussed in recent reviews (e.g., Kapp & DeCelles, 2019; Parsons et al., 2020; van Hinsbergen et al., 2019). However, we note that models proposing first collision of the Himalayan orogeny between India and an equatorial intra-oceanic arc at ∼61 Ma require two collisions at two separate subduction zones (an intra-oceanic subduction zone and a continental margin subduction zone) and therefore require two slab break-off events. We are unaware of any studies (including our own), which present bedrock evidence for more than one break-off event during the Himalayan orogeny.

Figure 10. The geodynamic significance of UHP exhumation for orogenesis and plate tectonics. (a and b) Schematic cartoon section of the India-Asia collision showing the postulated shallowing of Indian slab dip (e.g., Chen et al., 2022), marked by the onset of UHP exhumation at 47–46 Ma (not to scale). (a) Steep subduction and UHP metamorphism during onset of the India-Asia collision (∼50–47 Ma). Prior to collision, the Asian active continental margin represented an Accretionary Orogen (cf. Cawood et al., 2009) in which convergence was driven and accommodated by subduction of the Indian and/or Neotethys slab. (b) UHP exhumation and slab shallowing starting at 47–46 Ma, in response to the positive buoyancy of Indian continental crust following the onset of continental collision. The impacts of the reduced slab dip are annotated on (b), showing an increase in crustal shortening, Barrovian metamorphism, crustal contamination of arc magmatism and lower crustal melting of the Gangdese arc to produce adakite. The collision zone represents a Collisional Orogen (cf. Cawood et al., 2009), whereby convergence is accommodated by crustal shortening ± continental subduction and driven by subduction of the Australian slab to the east (see Section 6). Two alternative slab break-off scenarios are presented. Slab Scenario 1 (presented in (a)): UHP exhumation and slab dip shallowing occurred in response to slab break-off at 47–46 Ma. Slab Scenario 2 (presented in (b)): Alternatively, UHP exhumation occurred via detachment of the Tso Morari complex from the Indian slab, whilst the buoyancy of the Indian continental crust resulted in lateral slab dragging, overturning of the trailing oceanic slab and reduction in slab dip (see Parsons et al., 2021 for further discussion of lateral slab migrations during the India-Asia collision), with slab break-off occurring at a later time (see Section 6). (c) 46 Ma plate reconstruction showing tectonic events of the Eocene plate network reorganization, triggered by changes in the subduction dynamics of the India-Asia collision. UHP exhumation at 47–46 Ma provide a precise timestamp linking changes in the subduction dynamics of the India-Asia collision zone to plate kinematic changes of the wider plate network. Reconstruction drawn from Müller et al. (2019) using GPlates (Müller et al., 2018), with Greater India and Eurasian margin subduction zone outlines constrained by Parsons et al. (2020, 2021). Thick dashed black lines show present day locations of the Indus Suture Zone (ISZ) and Main Frontal Thrust (MFT) of the Himalayan orogen, requiring 1,000–2,000 km of crustal shortening since ∼47–46 Ma (Parsons et al., 2021). Abbreviations: AFR—African plate; ANT—Antarctic plate; AUS—Australian plate; CIR—Central Indian ridge; GI—Greater India; IND—Indian plate; ISZ—Indus Suture Zone; ja—Java; khl—Khoistan-Ladakh block; lh—Lhasa block; MFT—Main Frontal Thrust; mk—Mogok metamorphic belt; wb—West Burma block; WR—Wharton ridge.

6.2.4. UHP Exhumation During Eocene Plate Network Reorganization

From a plate-kinematic perspective (Figure 10c), UHP exhumation at 47–46 Ma coincides with a significant reorganization of the India-Eurasia-Australia plate network during the mid-Eocene (e.g., Gibbons et al., 2015; Parsons et al., 2021; Patriat & Achache, 1984). Key events during the reorganization (Figure 10c) included (a) a deceleration of Indian plate motion by 30%–38% between 45 and 40 Ma (Molnar & Stock, 2009); (b) reduction in spreading rate and clockwise rotation of spreading azimuth between India and Africa between 52 and 41 Ma (Cande et al., 2010; Patriat & Achache, 1984), followed by southwest jump of the Central India spreading ridge at ~41 Ma (Torsvik et al., 2013); (c) coupling of the Indian and Australian plates following a cessation of spreading on intervening Wharton ridge at ~43–36 Ma (Gibbons et al., 2015; Jacob et al., 2014); (d) onset of northward motion of the Australian plate at ~45–43 Ma, after being stationary since the mid-Cretaceous (Müller et al., 2019; Torsvik et al., 2008); (e) onset of subduction of the Australian plate beneath Java at 47–44 Ma (Smyth et al., 2008); and (f) acceleration of plate spreading between the Australian and Antarctic plates at ~47–45 Ma (Eagles, 2019; Torsvik et al., 2008).

Plate reconstructions and mantle tomographic analyses propose that this reorganization occurred in response to the India-Asia collision (Gibbons et al., 2015; Parsons et al., 2021; Replumaz et al., 2014); however, these studies lacked an unambiguous and precise marker linking the bedrock record of the collision to plate network reorganization. Crucially, our precise age constraint for the onset of UHP exhumation at 47–46 Ma corroborates those previous studies by demonstrating a viable, causative link between changes in the subduction dynamics of the India-Asia collision zone starting at 47–46 Ma (Figure 9) and the resulting mid-Eocene plate network reorganization that immediately followed (Figure 10c). Our synthesis of the bedrock record of metamorphism and magmatism during the Himalayan orogeny demonstrate that UHP exhumation was rapidly, and in some places immediately, followed by widespread, hotter, amphibolite facies metamorphism (Figure 9a), which we attribute to shallowing and underthrusting of the Indian plate beneath Eurasia. Consequently, we argue that our new geochronological constraints not only date the onset of UHP exhumation in the NW Himalaya, but also date the changes in subduction dynamics of the collision zone that triggered the Eocene plate network reorganization.

6.3. The Geodynamic Significance of UHP Exhumation for Orogenesis and Plate Tectonics

Our study demonstrates how our understanding of the bedrock record of continental collisions may be enriched by placing it within the context of plate kinematics. At the same time, the bedrock record provides a crucial means of ground truthing lithospheric- to planetary-scale models of plate tectonics and mantle geodynamics. Further understanding may therefore be gained through new applications of similar integrated approaches to other collision zones.

Multiple examples of HP and UHP metamorphism are recorded across much of SE Asia during the Early to Late Cretaceous, but their timing and tectonic significance is poorly constrained. This metamorphism broadly overlaps with multiple terrane accretion events from the region (e.g., Woyla, Southwest Borneo, and Argoland blocks Advokaat & van Hinsbergen, 2024; Hall, 2012; Metcalfe, 2021; Morley, 2012; van de Lagemaat & van Hinsbergen, 2024), as well as a previously recognized plate network reorganization at ~110–100 Ma (Matthews et al., 2012; Müller et al., 2016). Detailed petrochronology studies of these occurrences of HP/UHP metamorphism are yet to be conducted but may provide important constraints for plate reconstructions and orogenic models of SE Asia which continue to be debated and revised (e.g., Advokaat & van Hinsbergen, 2024; Hall, 2012; Metcalfe, 2021; Morley, 2012; van de Lagemaat & van Hinsbergen, 2024).

Further back in time, there are many examples HP and UHP metamorphic rocks associated with the Paleozoic tectonic evolution of the Rheic and Iapetus Oceans and related collisional events including the Caledonian, Scandian, and Grampian orogenies (see review of Domeier (2016)). The tectonic and geodynamic significance of these HP/UHP rocks is often unclear. Integrated petrochronology-plate kinematic analyses of these rocks may better constrain both the tectonometamorphic evolution of these HP/UHP metamorphic events and the plate kinematic evolution of the surrounding plate network (e.g., Bottrill et al., 2014; Domeier, 2016; Gilotti et al., 2008; Hacker et al., 2010). Whilst plate reconstructions of pre-Jurassic events are less well constrained than those of younger ages, integration of plate kinematics and bedrock data set still has potential to reveal new information for older tectonic events that would remain otherwise hidden when conducting either discipline (bedrock analysis or plate reconstruction modeling) in isolation.

7. Summary

By associating accessory phase ages with distinct metamorphic assemblages, and combining both high precision and high spatial resolution techniques, we demonstrate that the phase of peak zircon crystallization recorded in the Tso Morari complex at 47–46 Ma, corresponds to the onset of exhumation from UHP conditions. This study also describes the record of subduction-related major and accessory mineral growth preserved in a rare garnet-bearing Puga Gneiss, which records a part of the P-T-t history not preserved elsewhere. Zircon from a mafic eclogite have a U-Pb CA-ID-TIMS age of 46.912 ± 0.068 Ma (2σ) and an LA-ICPMS age of 47.5 ± 1.7 Ma, with REE profiles indicative of zircon crystallization at eclogite facies conditions. Those ages overlap with zircon rim ages (48.9 ± 1.2 Ma, LA-ICP-MS) and xenotime ages (47.4 ± 1.4 Ma; LA-ICP-MS) from the hosting Puga gneiss, which grew during breakdown of UHP garnet rims, as indicated by garnet element maps. Subsequent exhumation through the rutile closure temperature to crustal conditions is constrained by new dates of 40.4 ± 1.7 Ma and 36.3 ± 3.8 (2σ LA-ICP-MS).

The overlap between our mafic eclogite zircon ages and our xenotime-UHP garnet break down ages, indicate that the pulse of zircon growth recorded in the Tso Morari complex at 47–46 Ma (e.g., Donaldson et al., 2013) took place as a result of fluid infiltration at the onset of exhumation from UHP conditions, rather than as a result of peak UHP metamorphism. These ages from Tso Morari overlap with U-Pb ID-TIMS, SHRIMP, and SIMS analyses of zircon from eclogite-facies mafic rocks in Kaghan and Naran, ∼450–480 km to west of Tso Morari, which yielded ages of 46.4 ± 0.1, 46.2 ± 0.7, and 46 ± 2 Ma, respectively (Kaneko et al., 2003; Parrish et al., 2006; Zhang et al., 2022). We interpret this overlap as an indication that exhumation from UHP conditions occurred synchronously at 46–47 Ma across the whole of the NW Himalaya.

Integration of our new ages plus previously published ages from the NW Himalaya with existing metamorphic, magmatic, and plate kinematic constraints demonstrates that UHP exhumation at 47–46 Ma occurred in response to changes in subduction dynamics following the onset of the India-Asia collision (sensu stricto) between 50 and 47 Ma. Our data suggest that UHP exhumation was rapidly and in some places immediately followed by widespread, hotter, amphibolite facies metamorphism which we attribute to buoyancy-driven shallowing and under thrusting of the continental Indian slab beneath Eurasia beginning at 47–46 Ma. At a broader perspective, these changes in subduction dynamics and convergence mechanisms of the Himalayan orogeny (Figures 9a and 9b) also impacted the geodynamics and kinematics of the encompassing tectonic plate network.

Our new data from Tso Morari demonstrably tie the bedrock record of the Himalayan orogeny to slab dynamics and plate kinematics of the collision zone. Continent-continent collision of India and Asia at 50–47 Ma not only provided the trigger for UHP exhumation, but also resulted in, (a) significant changes in the metamorphic and magmatic evolution of the Himalayan orogen (Figure 9a); (b) the transition of the Himalaya from an accretionary orogen to a collisional orogen (Figure 9b); and (c) a significant reorganization of the wider India-Eurasia-Australia plate network (Figure 9c). Therefore, our new constraints not only date the onset of UHP exhumation in the NW Himalaya, but also date changes in subduction dynamics of the collision zone that triggered the Eocene plate network reorganization. As a proof-of-concept, our study demonstrates the value of integrated bedrock-plate kinematic approaches, which ultimately lead to a more holistic and accurate understanding how bedrock geology and plate tectonics are linked across subgrain to planetary scales.

Data Availability Statement

The EPMA (Bidgood, Gopon, et al., 2024), LA-ICPMS and ID-TIMS data (Bidgood, Roberts, et al., 2024) used for geochemistry analysis and U-Pb dating in this study has been uploaded to the Mendeley data repository with a DOI and an open access license CC BY 4.0.

References

Advokaat, E. L., & van Hinsbergen, D. J. J. (2024). Finding Argoland: Reconstructing a microcontinental archipelago from the SE Asian accretionary orogen. *Gondwana Research*, *128*, 161–263. https://doi.org/10.1016/j.gr.2023.10.005

Afonso, J. C., & Zlotnik, S. (2011). The subductability of continental lithosphere: The before and after story. *Arc-Continent Collision*, 53–86. https://doi.org/10.1007/978-3-540-88558-0_3

Ambrose, T. K., Larson, K. P., Guilmette, C., Cottle, J. M., Buckingham, H., & Rai, S. (2015). Lateral extrusion, underplating, and out-of-sequence thrusting within the Himalayan metamorphic core, Kanchenjunga, Nepal. *Lithosphere*, *7*(4), 441–464. https://doi.org/10.1130/L437.1

An, W., Hu, X., Garzanti, E., Wang, J.-G., & Liu, Q. (2021). New precise dating of the India-Asia collision in the Tibetan Himalaya at 61 Ma. *Geophysical Research Letters*, *48*(3), e2020GL090641. https://doi.org/10.1029/2020GL090641

Barley, M. E., Pickard, A. L., Zaw, K., Rak, P., & Doyle, M. G. (2003). Jurassic to Miocene magmatism and metamorphism in the Mogok metamorphic belt and the India-Eurasia collision in Myanmar. *Tectonics*, *22*(3). https://doi.org/10.1029/2002TC001398

Bidgood, A., Gopon, P., Waters, D., Roberts, N., & Parsons, A. (2024). Bidgood et al. 2024—Tso Morari—Supporting Information 2. EPMA methods and data [Dataset]. *Mendeley Data, V2*. https://doi.org/10.17632/vcfbxm6h9f.1

Bidgood, A., Roberts, N., Tapster, S., Waters, D., Parsons, A., & Gopon, P. (2024). Bidgood et al. 2024—Tso Morari—Supporting Information 3: Geochronology data [Dataset]. *Mendeley Data, V2*. https://doi.org/10.17632/t5fd58m67p.1

Bidgood, A. K. (2020). *The petrology and transformation history of continental crust in the Tso Morari Complex, Ladakh, Himalaya*. University of Oxford. Retrieved from https://ora.ox.ac.uk/objects/uuid:966a9121-82fc-4567-afbf-2bbcd55de04e

Bidgood, A. K., Parsons, A. J., Lloyd, G. E., Waters, D. J., & Goddard, R. M. (2021). EBSD-based criteria for coesite-quartz transformation. *Journal of Metamorphic Geology*, *39*(2), 165–180. https://doi.org/10.1016/j.jsg.2018.06.012

Bidgood, A. K., Waters, D. J., Dyck, B. J., & Roberts, N. M. W. (2023). The emplacement, alteration, subduction and metamorphism of met-agranites from the Tso Morari Complex, Ladakh Himalaya. *Mineralogical Magazine*, *87*(1), 40–59. https://doi.org/10.1180/mgm.2022.121

Bose, S., Schellart, W. P., Strak, V., Duarte, J. C., & Chen, Z. (2023). Sunda subduction drives ongoing India-Asia convergence. *Tectonophysics*, *849*, 229727. https://doi.org/10.1016/j.tecto.2023.229727

Bottrill, A. D., van Hunen, J., Cuthbert, S. J., Brueckner, H. K., & Allen, M. B. (2014). Plate rotation during continental collision and its relationship with the exhumation of UHP metamorphic terranes: Application to the Norwegian Caledonides. *Geochemistry, Geophysics, Geosystems*, *15*(5), 1766–1782. https://doi.org/10.1002/2014GC005253

Bouilhol, P., Jagoutz, O., Hanchar, J. M., & Dudas, F. O. (2013). Dating the India–Eurasia collision through arc magmatic records. *Earth and Planetary Science Letters*, *366*, 163–175. https://doi.org/10.1016/j.epsl.2013.01.023

Boutelier, D., & Cruden, A. R. (2018). Exhumation of (U) HP/LT rocks caused by diachronous slab breakoff. *Journal of Structural Geology*, *117*, 251–255. https://doi.org/10.1016/j.jsg.2018.06.012

Brun, J.-P., & Faccenna, C. (2008). Exhumation of high-pressure rocks driven by slab rollback. *Earth and Planetary Science Letters*, *272*(1–2), 1–7. https://doi.org/10.1016/j.epsl.2008.02.038

Buchs, N., & Epard, J. L. (2019). Geology of the eastern part of the Tso Morari nappe, the Nidar Ophiolite and the surrounding tectonic units (NW Himalaya, India). *Journal of Maps*, *15*(2), 38–48. https://doi.org/10.1080/17445647.2018.1541196

Burg, J.-P., & Bouilhol, P. (2019). Timeline of the South Tibet—Himalayan belt: The geochronological record of subduction, collision, and underthrusting from zircon and monazite U–Pb ages. *Canadian Journal of Earth Sciences*, *56*(12), 1318–1332. https://doi.org/10.1139/cjes-2018-0174

Burov, E., Francois, T., Agard, P., Le Pourhiet, L., Meyer, B., Tirel, C., et al. (2014). Rheological and geodynamic controls on the mechanisms of subduction and HP/UHP exhumation of crustal rocks during continental collision: Insights from numerical models. *Tectonophysics*, *631*, 212–250. https://doi.org/10.1016/j.tecto.2014.04.033

Cande, S. C., Patriat, P., & Dyment, J. (2010). Motion between the Indian, Antarctic and African plates in the early Cenozoic. *Geophysical Journal International*, *183*(1), 127–149. https://doi.org/10.1111/j.1365-246X.2010.04737.x

Capitanio, F. A., Replumaz, A., & Riel, N. (2015). Reconciling subduction dynamics during Tethys closure with large-scale Asian tectonics: Insights from numerical modelling. *Geochemistry, Geophysics, Geosystems*, *16*(3), 962–982. https://doi.org/10.1002/2014GC005660

Carosi, R., Montomoli, C., Iaccarino, S., Massonne, H.-J., Rubatto, D., Langone, A., et al. (2016). Middle to late Eocene exhumation of the Greater Himalayan Sequence in the Central Himalayas: Progressive accretion from the Indian plate. *GSA Bulletin*, *128*(11–12), 1571–1592. https://doi.org/10.1130/B31471.1

Carosi, R., Montomoli, C., Iaccarino, S., & Visonà, D. (2019). Structural evolution, metamorphism and melting in the Greater Himalayan Sequence in central-western Nepal. *Geological Society, London, Special Publications*, *483*(1), 305–323. https://doi.org/10.1144/SP483.3

Cawood, P. A., Kröner, A., Collins, W. J., Kusky, T. M., Mooney, W. D., & Windley, B. F. (2009). Accretionary orogens through Earth history. *Geological Society, London, Special Publications*, *318*, 1–36. https://doi.org/10.1144/SP318.1

Chen, R. X., & Zheng, Y. F. (2017). Metamorphic zirconology of continental subduction zones. *Journal of Asian Earth Sciences*, *145*, 149–176. https://doi.org/10.1016/j.jseaes.2017.04.029

Chen, R. X., Zheng, Y. F., & Xie, L. (2010). Metamorphic growth and recrystallization of zircon: Distinction by simultaneous in-situ analyses of trace elements, U–Th–Pb and Lu–Hf isotopes in zircons from eclogite-facies rocks in the Sulu orogen. *Lithos*, *114*(1–2), 132–154. https://doi.org/10.1016/J.LITHOS.2009.08.006

Chen, S., Chen, Y., Guillot, S., & Li, Q. (2022). Change in subduction dip angle of the Indian continental lithosphere inferred from the western Himalayan eclogites. *Frontiers in Earth Science*, *9*. https://doi.org/10.3389/feart.2021.790999

Cherniak, D., Watson, E., & Wark, D. (2007). Ti diffusion in quartz. *Chemical Geology*, *236*(1–2), 65–74. https://doi.org/10.1016/j.chemgeo.2006.09.001

Cherniak, D. J. (2000). Pb diffusion in rutile. *Contributions to Mineralogy and Petrology*, *139*(2), 198–207. https://doi.org/10.1007/PL00007671

Chew, D. M., Petrus, J. A., & Kamber, B. S. (2014). U–Pb LA–ICPMS dating using accessory mineral standards with variable common Pb. *Chemical Geology*, *363*, 185–199. https://doi.org/10.1016/j.chemgeo.2013.11.006

Condon, D. J., Schoene, B., McLean, N. M., Bowring, S. A., & Parrish, R. R. (2015). Metrology and traceability of U–Pb isotope dilution geochronology (EARTHTIME Tracer Calibration Part I). *Geochimica et Cosmochimica Acta*, *164*, 464–480. https://doi.org/10.1016/J.GCA.2015.05.026

de Sigoyer, J., Chavagnac, V., Blichert-Toft, J., Villa, I. M., Luais, B., Guillot, S., et al. (2000). Dating the Indian continental subduction and collisional thickening in the northwest Himalaya: Multichronology of the Tso Morari eclogites. *Geology*, *28*(6), 487–490. https://doi.org/10.1130/0091-7613(2000)28<487:DTICSA>2.0.CO;2

de Sigoyer, J., Guillot, S., Lardeaux, J. M., & Mascle, G. (1997). Glaucophane-bearing eclogites in the Tso Morari dome (eastern Ladakh, NW Himalaya). *European Journal of Mineralogy*, *128*(2–3), 197–212. https://doi.org/10.1127/ejm/9/5/1073

Ding, H., Zhang, Z., Dong, X., Tian, Z., Xiang, H., Mu, H., et al. (2016). Early Eocene (c. 50 Ma) collision of the Indian and Asian continents: Constraints from the North Himalayan metamorphic rocks, southeastern Tibet. *Earth and Planetary Science Letters*, *435*, 64–73. https://doi.org/10.1016/j.epsl.2015.12.006

Domeier, M. (2016). A plate tectonic scenario for the Iapetus and Rheic oceans. *Gondwana Research*, *36*, 275–295. https://doi.org/10.1016/j.gr.2015.08.003

Donaldson, D. G., Webb, A. A. G., Menold, C. A., Kylander-Clark, A. R. C., & Hacker, B. R. (2013). Petrochronology of Himalayan ultrahigh-pressure eclogite. *Geology*, *41*(8), 835–838. https://doi.org/10.1130/G33699.1

Doubrovine, P. V., Steinberger, B., & Torsvik, T. H. (2012). Absolute plate motions in a reference frame defined by moving hot spots in the Pacific, Atlantic, and Indian oceans. *Journal of Geophysical Research*, *117*(B9), B09101. https://doi.org/10.1029/2011JB009072

Dutta, D., & Mukherjee, S. (2021). Extrusion kinematics of UHP terrane in a collisional orogen: EBSD and microstructure-based approach from the Tso Morari Crystallines (Ladakh Himalaya). *Tectonophysics*, *800*, 228641. https://doi.org/10.1016/j.tecto.2020.228641

Eagles, G. (2019). A little spin in the Indian Ocean plate circuit. *Tectonophysics*, *754*, 80–100. https://doi.org/10.1016/j.tecto.2019.01.015

Epard, J., & Steck, A. (2008). Structural development of the Tso Morari ultra-high pressure nappe of the Ladakh Himalaya. *Tectonophysics*, *451*(1–4), 242–264. https://doi.org/10.1016/j.tecto.2007.11.050

Ferry, J. M., & Watson, E. B. (2007). New thermodynamic models and revised calibrations for the Ti-in-zircon and Zr-in-rutile thermometers. *Contributions to Mineralogy and Petrology*, *154*(4), 429–437. https://doi.org/10.1007/s00410-007-0201-0

Foster, G., Parrish, R. R., Horstwood, M. S., Chenery, S., Pyle, J., & Gibson, H. D. (2004). The generation of prograde P–T–t points and paths; a textural, compositional, and chronological study of metamorphic monazite. *Earth and Planetary Science Letters*, *228*(1–2), 125–142. https://doi.org/10.1016/j.epsl.2004.09.024

Fuchs, G., & Linner, M. (1996). On the geology of the suture zone and Tso Morari dome in eastern Ladakh (Himalaya). *Jahrbuch Der Geologischen Bundesanstalt*, *139*(191), 207.

Gansser, A. (1966). The Indian Ocean and the Himalayas, a geological interpretation. *Eclogae Geologicae Helvetiae*, *67*, 479–507.

Garzanti, E., Radeff, G., & Malusà, M. G. (2018). Slab breakoff: A critical appraisal of a geological theory as applied in space and time. *Earth-Science Reviews*, *177*, 303–319. https://doi.org/10.1016/j.earscirev.2017.11.012

Gibbons, A. D., Zahirovic, S., Müller, R. D., Whittaker, J. M., & Yatheesh, V. (2015). A tectonic model reconciling evidence for the collisions between India, Eurasia and intra-oceanic arcs of the central-eastern Tethys. *Gondwana Research*, *28*(2), 451–492. https://doi.org/10.1016/j.gr.2015.01.001

Gilotti, J. A., Jones, K. A., Elvevold, S., Higgins, A. K., Gilotti, J. A., & Smith, M. P. (2008). *Caledonian metamorphic patterns in Greenland. The Greenland Caledonides: Evolution of the northeast margin of Laurentia* (Vol. 202). Geological Society of America. https://doi.org/10.1130/2008.1202(08)

Girard, M. (2001). Metamorphism and tectonics of the transition between non metamorphic Tethyan Himalaya sediments and the North Himalayan Crystalline Zone (Rupshuarea, Ladakh, NW India). *Section Des Sciences de La Terre de l'université*. http://www.unil.ch/files/live/sites/iste/files/shared/X.Library/MemoirsofGeology/35–Girard

Girard, M., & Bussy, F. (1999). Late Pan-African magmatism in the Himalaya: New geochronological and geochemical data from the Ordovician Tso Morari metagranites (Ladakh, NW India). *Schweizerische Mineralogische Und Petrographische Mitteilungen*, *79*, 399–418. https://doi.org/10.5169/seals-60215

Goscombe, B., Gray, D., & Foster, D. A. (2018). Metamorphic response to collision in the Central Himalayan Orogen. *Gondwana Research*, *57*, 191–265. https://doi.org/10.1016/j.gr.2018.02.002

Guan, Q., Zhu, D.-C., Zhao, Z.-D., Dong, G.-C., Zhang, L.-L., Li, X.-W., et al. (2012). Crustal thickening prior to 38Ma in southern Tibet: Evidence from lower crust-derived adakitic magmatism in the Gangdese Batholith. *Gondwana Research*, *21*(1), 88–99. https://doi.org/10.1016/j.gr.2011.07.004

Guillot, S., Hattori, K., Agard, P., Schwartz, S., & Vidal, O. (2009). *Exhumation processes in oceanic and continental subduction contexts: A review* (pp. 175–205). Springer Berlin Heidelberg. Retrieved from https://link.springer.com/chapter/10.1007/978-3-540-87974-9_10

Guillot, S., Mahéo, G., de Sigoyer, J., Hattori, K. H., & Pêcher, A. (2008). Tethyan and Indian subduction viewed from the Himalayan high- to ultrahigh-pressure metamorphic rocks. *Tectonophysics*, *451*(1–4), 225–241. https://doi.org/10.1016/j.tecto.2007.11.059

Guillot, S., Sigoyer, J. D., Lardeaux, J., & Mascle, G. (1997). Eclogitic metasediments from the Tso Morari area (Ladakh, Himalaya): Evidence for continental subduction during India-Asia convergence. *Contributions to Mineralogy and Petrology*, *128*(2–3), 197–212. https://doi.org/10.1007/s004100050303

Gürer, D., Granot, R., & van Hinsbergen, D. J. J. (2022). Plate tectonic chain reaction revealed by noise in the Cretaceous quiet zone. *Nature Geoscience*, *15*(3), 233–239. https://doi.org/10.1038/s41561-022-00893-7

Hacker, B. R., Andersen, T. B., Johnston, S., Kylander-Clark, A. R. C., Peterman, E. M., Walsh, E. O., & Young, D. (2010). High-temperature deformation during continental-margin subduction & exhumation: The ultrahigh-pressure Western Gneiss Region of Norway. *Tectonophysics*, *480*(1–4), 149–171. https://doi.org/10.1016/j.tecto.2009.08.012

Hacker, B. R., & Gerya, T. V. (2013). Paradigms, new and old, for ultrahigh-pressure tectonism. *Tectonophysics*, *603*, 79–88. https://doi.org/10.1016/j.tecto.2013.05.026

Hall, R. (2012). Late Jurassic–Cenozoic reconstructions of the Indonesian region and the Indian Ocean. *Tectonophysics*, *570–571*, 1–41. https://doi.org/10.1016/j.tecto.2012.04.021

Harrison, T. M., Célérier, J., Aikman, A. B., Hermann, J., & Heizler, M. T. (2009). Diffusion of [40]Ar in muscovite. *Geochimica et Cosmochimica Acta*, *73*(4), 1039–1051. https://doi.org/10.1016/j.gca.2008.09.038

Harrison, T. M., Duncan, I. A. N., & Mcdougall, I. A. N. (1985). Diffusion of [40]Ar in biotite: Temperature, pressure and compositional effects. *Geochimica et Cosmochimica Acta*, *49*(11), 2461–2468. https://doi.org/10.1016/0016-7037(85)90246-7

Horstwood, M. S., Košler, J., Gehrels, G., Jackson, S. E., McLean, N. M., Paton, C., et al. (2016). Community-derived standards for LA-ICP-MS U-(Th-) Pb geochronology–Uncertainty propagation, age interpretation and data reporting. *Geostandards and Geoanalytical Research*, *40*(3), 311–332. https://doi.org/10.1111/j.1751-908X.2016.00379.x

Hu, X., Garzanti, E., Moore, T., & Raffi, I. (2015). Direct stratigraphic dating of India-Asia collision onset at the Selandian (middle Paleocene, 59±1 Ma). *Geology*, *43*(10), 859–862. https://doi.org/10.1130/G36872.1

Hu, X., Garzanti, E., Wang, J., Huang, W., An, W., & Webb, A. (2016). The timing of India-Asia collision onset—Facts, theories, controversies. *Earth-Science Reviews*, *160*, 264–299. https://doi.org/10.1016/j.earscirev.2016.07.014

Ingalls, M., Rowley, D. B., Currie, B., & Colman, A. S. (2016). Large-scale subduction of continental crust implied by India–Asia mass-balance calculation. *Nature Geoscience*, *9*(11), 848–853. https://doi.org/10.1038/ngeo2806

Jacob, J., Dyment, J., & Yatheesh, V. (2014). Revisiting the structure, age, and evolution of the Wharton Basin to better understand subduction under Indonesia. *Journal of Geophysical Research: Solid Earth*, *119*(1), 169–190. https://doi.org/10.1002/2013JB010285

Jagoutz, O., Bouilhol, P., Schaltegger, U., & Müntener, O. (2019). The isotopic evolution of the Kohistan Ladakh arc from subduction initiation to continent arc collision. *Geological Society, London, Special Publications*, *483*(1), 165–182. https://doi.org/10.1144/SP483.7

Ji, M., Gao, X.-Y., Xia, Q.-X., & Zheng, Y.-F. (2024). Secular change of metamorphic features in the Himalayan orogen during the Cenozoic and its tectonic implications. *Earth-Science Reviews*, *248*, 104640. https://doi.org/10.1016/j.earscirev.2023.104640

Jonnalagadda, M. K., Karmalkar, N. R., Duraiswami, R. A., Harshe, S., Gain, S., & Griffin, W. L. (2017). Formation of atoll garnets in the UHP eclogites of the Tso Morari Complex, Ladakh, Himalaya. *Journal of Earth System Science*, *126*(8), 107. https://doi.org/10.1007/s12040-017-0887-y

Kaneko, Y., Katayama, I., Yamamoto, H., Misawa, K., Ishikawa, M., Rehman, H. U., et al. (2003). Timing of Himalayan ultrahigh-pressure metamorphism: Sinking rate and subduction angle of the Indian continental crust beneath Asia. *Journal of Metamorphic Geology*, *21*(6), 589–599. https://doi.org/10.1046/j.1525-1314.2003.00466.x

Kapp, P., & DeCelles, P. G. (2019). Mesozoic–Cenozoic geological evolution of the Himalayan-Tibetan orogen and working tectonic hypotheses. *American Journal of Science*, *319*(3), 159–254. https://doi.org/10.2475/03.2019.01

Kohn, M. J., Corrie, S. L., & Markley, C. (2015). The fall and rise of metamorphic zircon. *American Mineralogist*, *100*(4), 897–908. https://doi.org/10.2138/AM-2015-5064

Kohn, M. J., Engi, M., & Lanari, P. (2017). Petrochronology. *Methods and Applications, Mineralogical Society of America Reviews in Mineralogy and Geochemistry*, *83*(1), 575. https://doi.org/10.1515/9783110561890

Kooijman, E., Mezger, K., & Berndt, J. (2010). Constraints on the U–Pb systematics of metamorphic rutile from in situ LA-ICP-MS analysis. *Earth and Planetary Science Letters*, *293*(3–4), 321–330. https://doi.org/10.1016/j.epsl.2010.02.047

Kylander-Clark, A. R. C., Hacker, B. R., & Mattinson, J. M. (2008). Slow exhumation of UHP terranes: Titanite and rutile ages of the Western Gneiss Region, Norway. *Earth and Planetary Science Letters*, *272*(3–4), 531–540. https://doi.org/10.1016/j.epsl.2008.05.019

Laik, A., Schellart, W. P., & Strak, V. (2022). Sustained indentation in 2-D models of continental collision involving whole mantle subduction. *Geophysical Journal International*, *232*(1), 343–365. https://doi.org/10.1093/gji/ggac339

Lamont, T. N., Searle, M. P., Hacker, B. R., Htun, K., Htun, K. M., Morley, C. K., et al. (2021). Late Eocene-Oligocene granulite facies garnet-sillimanite migmatites from the Mogok Metamorphic belt, Myanmar, and implications for timing of slip along the Sagaing Fault. *Lithos*, *386–387*, 106027. https://doi.org/10.1016/j.lithos.2021.106027

Leech, M. L., Singh, S., & Jain, A. K. (2007). Continuous metamorphic zircon growth and interpretation of U-Pb SHRIMP dating: An example from the Western Himalaya. *International Geology Review*, *49*(4), 313–328. https://doi.org/10.2747/0020-6814.49.4.313

Le Fort, P. (1975). Himalayas: The collided range. Present knowledge of the continental arc. *American Journal of Science*, *275*, 1–44.

Li, C., van der Hilst, R. D., Meltzer, A. S., & Engdahl, E. R. (2008). Subduction of the Indian lithosphere beneath the Tibetan Plateau and Burma. *Earth and Planetary Science Letters*, *274*(1–2), 157–168. https://doi.org/10.1016/j.epsl.2008.07.016

Li, Q. L., Yang, Y. N., Shi, Y. H., & Lin, W. (2013). Eclogite rutile U-Pb dating: Constraint for formation and evolution of continental collisional orogen. *Chinese Science Bulletin*, *58*(23), 2279–2284.

Little, T. A., Hacker, B. R., Gordon, S. M., Baldwin, S. L., Fitzgerald, P. G., Ellis, S., & Korchinski, M. (2011). Diapiric exhumation of Earth's youngest (UHP) eclogites in the gneiss domes of the D'Entrecasteaux Islands, Papua New Guinea. *Tectonophysics*, *510*(1–2), 39–68. https://doi.org/10.1016/j.tecto.2011.06.006

Long, S. P., Kohn, M. J., Kerswell, B. C., Starnes, J. K., Larson, K. P., Blackford, N. R., & Soignard, E. (2020). Thermometry and microstructural analysis imply protracted extensional exhumation of the Tso Morari UHP nappe, northwestern Himalaya: Implications for models of UHP exhumation. *Tectonics*, *39*(12), e2020TC006482. https://doi.org/10.1029/2020TC006482

Lotout, C., Pitra, P., Poujol, M., Anczkiewicz, R., & Van Den Driessche, J. (2018). Timing and duration of Variscan high-pressure metamorphism in the French Massif Central: A multimethod geochronological study from the Najac Massif. *Lithos*, *308*, 381–394. https://doi.org/10.1016/j.lithos.2018.03.022

Ma, L., Wang, B.-D., Jiang, Z.-Q., Wang, Q., Li, Z.-X., Wyman, D. A., et al. (2014). Petrogenesis of the Early Eocene adakitic rocks in the Napuri area, southern Lhasa: Partial melting of thickened lower crust during slab break-off and implications for crustal thickening in southern Tibet. *Lithos*, *196–197*, 321–338. https://doi.org/10.1016/j.lithos.2014.02.011

Matthews, K. J., Seton, M., & Müller, R. D. (2012). A global-scale plate reorganization event at 105−100Ma. *Earth and Planetary Science Letters*, *355–356*, 283–298. https://doi.org/10.1016/j.epsl.2012.08.023

Metcalfe, I. (2021). Multiple Tethyan ocean basins and orogenic belts in Asia. *Gondwana Research*, *100*, 87–130. https://doi.org/10.1016/j.gr.2021.01.012

Mezger, K., Hanson, G., & SR, B. (1989). High-precision UPb ages of metamorphic rutile: Application to the cooling history of high-grade terranes. *Earth and Planetary Science Letters*, *96*(1–2), 106–118. https://doi.org/10.1016/0012-821X(89)90126-X

Möller, C., Andersson, J., Dyck, B., & Antal Lundin, I. (2015). Exhumation of an eclogite terrane as a hot migmatitic nappe, Sveconorwegian orogen. *Lithos*, *226*, 147–168. https://doi.org/10.1016/J.LITHOS.2014.12.013

Molnar, P., & Stock, J. M. (2009). Slowing of India's convergence with Eurasia since 20 Ma and its implications for Tibetan mantle dynamics. *Tectonics*, *28*(3). https://doi.org/10.1029/2008TC002271

Morley, C. K. (2012). Late Cretaceous–early Palaeogene tectonic development of SE Asia. *Earth-Science Reviews*, *115*(1–2), 37–75. https://doi.org/10.1016/j.earscirev.2012.08.002

Mottram, C. M., Cottle, J. M., & Kylander-Clark, A. R. C. (2019). Campaign-style U-Pb titanite petrochronology: Along-strike variations in timing of metamorphism in the Himalayan metamorphic core. *Geoscience Frontiers*, *10*(3), 827–847. https://doi.org/10.1016/j.gsf.2018.09.007

Müller, R. D., Cannon, J., Qin, X., Watson, R. J., Gurnis, M., Williams, S., et al. (2018). GPlates: Building a virtual Earth through deep time. *Geochemistry, Geophysics, Geosystems*, *19*(7), 2243–2261. https://doi.org/10.1029/2018GC007584

Müller, R. D., Seton, M., Zahirovic, S., Williams, S. E., Matthews, K. J., Wright, N. M., et al. (2016). Ocean basin evolution and global-scale plate reorganization events since Pangea breakup. *Annual Review of Earth and Planetary Sciences*, *44*(1), 107–138. https://doi.org/10.1146/annurev-earth-060115-012211

Müller, R. D., Zahirovic, S., Williams, S. E., Cannon, J., Seton, M., Bower, D. J., et al. (2019). A global plate model including lithospheric deformation along major rifts and orogens since the Triassic. *Tectonics*, *38*(6), 1884–1907. https://doi.org/10.1029/2018TC005462

O'Brien, P., & Sachan, H. (2000). Diffusion modelling in garnet from Tso Morari eclogite and implications for exhumation models. *Earth Science Frontiers*, *7*, 25–27. http://d.wanfangdata.com.cn/periodical_dxqy2000z1010.aspx

O'Brien, P. J. (2006). The age of deep, steep continental subduction in the NW Himalaya: Relating zircon growth to metamorphic history. Comment on: "The onset of India–Asia continental collision: Early, steep subduction required by the timing of UHP metamorphism in the western. *Earth and Planetary Science Letters*, *245*(3–4), 814–816. https://doi.org/10.1016/j.epsl.2006.03.033

O'Brien, P. J. (2019). Eclogites and other high-pressure rocks in the Himalaya: A review. *Geological Society, London, Special Publications*, *483*(1), 183–213. https://doi.org/10.1144/sp483.13

O'Brien, P. J. (2019a). Eclogites and other high-pressure rocks in the Himalaya: A review. *Geological Society, London, Special Publications*, *483*(1), 183–213. https://doi.org/10.1144/SP483.13

O'Brien, P. J. (2019b). Tso Morari coesite eclogite: Pseudosection predictions v. the preserved record and implications for tectonometamorphic models. *Geological Society, London, Special Publications*, *474*(1), 5–24. https://doi.org/10.1144/SP474.16

O'Brien, P. J., Zotov, N., Law, R. D., Khan, M. A., & Jan, M. Q. (2001). Coesite in Himalayan eclogite and implications for models of India-Asia collision. *Geology*, *29*(5), 435–438. https://doi.org/10.1130/0091-7613(2001)029<0435:CIHEAI>2.0.CO;2

Oriolo, S., Wemmer, K., Oyhantçabal, P., Fossen, H., Schulz, B., & Siegesmund, S. (2018). Geochronology of shear zones–A review. *Earth-Science Reviews*, *185*, 665–683. https://doi.org/10.1016/j.earscirev.2018.07.007

Palin, R. M., Searle, M. P., St-Onge, M. R., Waters, D. J., Roberts, N. M. W., Horstwood, M. S. A., et al. (2014). Monazite geochronology and petrology of kyanite- and sillimanite-grade migmatites from the northwestern flank of the eastern Himalayan syntaxis. *Gondwana Research*, *26*(1), 323–347. https://doi.org/10.1016/j.gr.2013.06.022

Palin, R. M., Searle, M. P., Waters, D. J., Horstwood, M. S. A., & Parrish, R. R. (2012). Combined thermobarometry and geochronology of peraluminous metapelites from the Karakoram metamorphic complex, North Pakistan; New insight into the tectonothermal evolution of the Baltoro and Hunza Valley regions. *Journal of Metamorphic Geology*, *30*(8), 793–820. https://doi.org/10.1111/j.1525-1314.2012.00999.x

Palin, R. M., St-Onge, M. R., Waters, D. J., Searle, M. P., & Dyck, B. (2014). Phase equilibria modelling of retrograde amphibole and clinozoisite in mafic eclogite from the Tso Morari massif, northwest India: Constraining the P–T–M (H_2O) conditions of exhumation. *Journal of Metamorphic Geology*, *32*(7), 675–693. https://doi.org/10.1111/jmg.12085

Parrish, R., Gough, S., Searle, M., & Waters, D. (2006). Plate velocity exhumation of ultrahigh-pressure eclogites in the Pakistan Himalaya. *Geology*, *34*(11), 989–992. https://doi.org/10.1130/G22796A.1

Parsons, A. J., Hosseini, K., Palin, R. M., & Sigloch, K. (2020). Geological, geophysical and plate kinematic constraints for models of the India-Asia collision and the post-Triassic central Tethys oceans. *Earth-Science Reviews*, *208*, 103084. https://doi.org/10.1016/j.earscirev.2020.103084

Parsons, A. J., Sigloch, K., & Hosseini, K. (2021). Australian plate subduction is responsible for northward motion of the India-Asia collision zone and ∼1,000 km lateral migration of the Indian slab. *Geophysical Research Letters*, *48*(18), e2021GL094904. https://doi.org/10.1029/2021GL094904

Passchier, C. W., & Trouw, R. A. J. (2005). Deformation mechanisms. In *Microtectonics* (pp. 25–66). Springer-Verlag. https://doi.org/10.1007/3-540-29359-0_3

Patriat, P., & Achache, J. (1984). India–Eurasia collision chronology has implications for crustal shortening and driving mechanism of plates. *Nature*, *311*(5987), 615–621. https://doi.org/10.1038/311615a0

Piazolo, S., Belousova, E., La Fontaine, A., Corcoran, C., & Cairney, J. M. (2017). Trace element homogeneity from micron- to atomic scale: Implication for the suitability of the zircon GJ-1 as a trace element reference material. *Chemical Geology*, *456*, 10–18. https://doi.org/10.1016/J.CHEMGEO.2017.03.001

Regis, D., Warren, C. J., Mottram, C. M., & Roberts, N. M. (2016). Using monazite and zircon petrochronology to constrain the P–T–t evolution of the middle crust in the Bhutan Himalaya. *Journal of Metamorphic Geology*, *34*(6), 617–639. https://doi.org/10.1111/jmg.12196

Replumaz, A., Capitanio, F. A., Guillot, S., Negredo, A. M., & Villaseñor, A. (2014). The coupling of Indian subduction and Asian continental tectonics. *Gondwana Research*, *26*(2), 608–626. https://doi.org/10.1016/j.gr.2014.04.003

Roberts, N. M., Thomas, R. J., & Jacobs, J. (2016). Geochronological constraints on the metamorphic sole of the Semail ophiolite in the United Arab Emirates. *Geoscience Frontiers*, *7*(4), 609–619. https://doi.org/10.1016/j.gsf.2015.12.003

Rubatto, D. (2002). Zircon trace element geochemistry: Partitioning with garnet and the link between U–Pb ages and metamorphism. *Chemical Geology*, *184*(1), 123–138. https://doi.org/10.1016/S0009-2541(01)00355-2

Rubatto, D., & Hermann, J. (2003). Zircon formation during fluid circulation in eclogites (Monviso, Western Alps): Implications for Zr and Hf budget in subduction zones. *Geochimica et Cosmochimica Acta*, *67*(12), 2173–2187. https://doi.org/10.1016/S0016-7037(02)01321-2

Sachan, H. K., Mukherjee, B. K., Ogasawara, Y., Maruyama, S., Ishida, H., Muko, A., & Yoshioka, N. (2004). Discovery of coesite from Indus Suture Zone (ISZ), Ladakh, India: Evidence for deep subduction. *European Journal of Mineralogy*, *16*(2), 235–240. https://doi.org/10.1127/0935-1221/2004/0016-0235

Schaltegger, U., Fanning, C. M., Günther, D., Maurin, J. C., Schulmann, K., & Gebauer, D. (1999). Growth, annealing and recrystallization of zircon and preservation of monazite in high-grade metamorphism: Conventional and in-situ U-Pb isotope, cathodoluminescence and micro-chemical evidence. *Contributions to Mineralogy and Petrology*, *134*(2–3), 186–201. https://doi.org/10.1007/s004100050478

Schlup, M., Carter, A., Cosca, M., & Steck, A. (2003). Exhumation history of eastern Ladakh revealed by ${}^{40}Ar/{}^{39}Ar$ and fission-track ages: The Indus River–Tso Morari transect, NW Himalaya. *Journal of the Geological Society*, *3*, 385–399. https://doi.org/10.1144/0016-764902-084

Schlup, M., Carter, A., Cosca, M., & Steck, A. (2003). Exhumation history of eastern Ladakh revealed by ${}^{40}Ar/{}^{39}Ar$ and fission-track ages: The Indus River–Tso Morari transect, NW Himalaya. *Journal of the Geological Society*, *160*(3), 385–399. https://doi.org/10.1144/0016-764902-084

Schwartz, S., Lardeaux, J. M., Tricart, P., Guillot, S., & Labrin, E. (2007). Diachronous exhumation of HP–LT metamorphic rocks from south-western Alps: Evidence from fission-track analysis. *Terra Nova*, *19*(2), 133–140. https://doi.org/10.1111/J.1365-3121.2006.00728.X

Searle, M. P. (2019). Timing of subduction initiation, arc formation, ophiolite obduction and India–Asia collision in the Himalaya. *Geological Society, London, Special Publications*, *483*(1), 19–37. https://doi.org/10.1144/SP483.8

Searle, M. P., Elliott, J. R., Phillips, R. J., & Chung, S.-L. (2011). Crustal–lithospheric structure and continental extrusion of Tibet. *Journal of the Geological Society*, *168*(3), 633–672. https://doi.org/10.1144/0016-76492010-139

Searle, M. P., Garber, J. M., Hacker, B. R., Htun, K., Gardiner, N. J., Waters, D. J., & Robb, L. J. (2020). Timing of syenite-charnockite magmatism and ruby and sapphire metamorphism in the Mogok Valley Region, Myanmar. *Tectonics*, *39*(3), e2019TC005998. https://doi.org/10.1029/2019TC005998

Searle, M. P., Morley, C. K., Waters, D. J., Gardiner, N. J., Htun, U. K., Nu, T. T., & Robb, L. J. (2017). Chapter 12 tectonic and metamorphic evolution of the Mogok Metamorphic and Jade Mines belts and ophiolitic terranes of Burma (Myanmar). *Geological Society, London, Memoirs*, *48*(1), 261–293. https://doi.org/10.1144/M48.12

Searle, M. P., Noble, S. R., Cottle, J. M., Waters, D. J., Mitchell, A. H. G., Hlaing, T., & Horstwood, M. S. A. (2007). Tectonic evolution of the Mogok metamorphic belt, Burma (Myanmar) constrained by U-Th-Pb dating of metamorphic and magmatic rocks. *Tectonics*, *26*(3). https://doi.org/10.1029/2006TC002083

Sheng, Y. M., Zheng, Y. F., Chen, R. X., Li, Q., & Dai, M. (2012). Fluid action on zircon growth and recrystallization during quartz veining within UHP eclogite: Insights from U–Pb ages, O–Hf isotopes and trace elements. *Lithos*, *136–139*, 126–144. https://doi.org/10.1016/J.LITHOS.2011.06.012

Sinha Roy, S. (1976). A possible Himalayan microcontinent. *Nature*, *263*(5573), 117–120. https://doi.org/10.1038/263117a0

Skuzovatov, S. Y., Shatsky, V. S., Ragozin, A. L., & Wang, K. L. (2021). Ubiquitous post-peak zircon in an eclogite from the Kumdy-Kol, Kokchetav UHP-HP Massif (Kazakhstan): Significance of exhumation-related zircon growth and modification in continental-subduction settings. *Island Arc*, *30*(1), e12385. https://doi.org/10.1111/IAR.12385

Smit, M. A., Hacker, B. R., & Lee, J. (2014). Tibetan garnet records early Eocene initiation of thickening in the Himalaya. *Geology*, *42*(7), 591–594. https://doi.org/10.1130/G35524.1

Smyth, H. R., Hall, R., Nichols, G. J., Draut, A. E., Clift, P. D., & Scholl, D. W. (2008). Cenozoic volcanic arc history of East Java, Indonesia: The stratigraphic record of eruptions on an active continental margin. Formation and Applications of the Sedimentary Record in Arc Collision Zones. *Geological Society of America*, *436*, 0. https://doi.org/10.1130/2008.2436(10)

Soret, M., Larson, K. P., Cottle, J., & Ali, A. (2021). How Himalayan collision stems from subduction. *Geology*, *49*(8), 894–898. https://doi.org/10.1130/g48803.1

Stacey, J. T., & Kramers, J. D. (1975). Approximation of terrestrial lead isotope evolution by a two-stage model. *Earth and Planetary Science Letters*, *26*(2), 207–221. https://doi.org/10.1016/0012-821x(75)90088-6

Stampfli, G. M., & Borel, G. D. (2004). The TRANSMED transects in space and time: Constraints on the paleotectonic evolution of the Mediterranean domain. In W. Cavazza, F. Roure, W. Spakman, G. M. Stampfli, & P. A. Ziegler (Eds.), *The TRANSMED Atlas. The Mediterranean region from crust to mantle: Geological and geophysical framework of the Mediterranean and the surrounding areas* (pp. 53–80). Springer. https://doi.org/10.1007/978-3-642-18919-7_3

Steck, A., Epard, J. L., Vannay, J. C., Hunziker, J., Girard, M., Morard, A., & Robyr, M. (1998). Geological transect across the Tso Morari and Spiti areas: The nappe structures of the Tethys Himalaya. *Eclogae Geologicae Helvetiae*, *91*, 103–121.

Stipp, M., Stünitz, H., Heilbronner, R., & Schmid, S. M. (2002). Dynamic recrystallization of quartz: Correlation between natural and experimental conditions. *Geological Society, London, Special Publications*, *200*(1), 171–190. https://doi.org/10.1144/gsl.sp.2001.200.01.11

St-Onge, M. R., Rayner, N., Palin, R. M., Searle, M. P., & Waters, D. J. (2013). Integrated pressure—Temperature—time constraints for the Tso Morari dome (Northwest India): Implications for the burial and exhumation path of UHP units in the western Himalaya. *Journal of Metamorphic Geology*, *31*(5), 469–504. https://doi.org/10.1111/jmg.12030

Szymanowski, D., Fehr, M. A., Guillong, M., Coble, M. A., Wotzlaw, J. F., Nasdala, L., et al. (2018). Isotope-dilution anchoring of zircon reference materials for accurate Ti-in-zircon thermometry. *Chemical Geology*, *481*, 146–154. https://doi.org/10.1016/j.chemgeo.2018.02.001

Tapster, S., Condon, D. J., Naden, J., Noble, S. R., Petterson, M. G., Roberts, N. M. W., et al. (2016). Rapid thermal rejuvenation of high-crystallinity magma linked to porphyry copper deposit formation; evidence from the Koloula Porphyry Prospect, Solomon Islands. *Earth and Planetary Science Letters*, *442*, 206–217. https://doi.org/10.1016/J.EPSL.2016.02.046

Torsvik, T. H., Amundsen, H., Hartz, E. H., Corfu, F., Kusznir, N., Gaina, C., et al. (2013). A Precambrian microcontinent in the Indian Ocean. *Nature Geoscience*, *6*(3), 223–227. https://doi.org/10.1038/ngeo1736

Torsvik, T. H., Müller, R. D., Van der Voo, R., Steinberger, B., & Gaina, C. (2008). Global plate motion frames: Toward a unified model. *Reviews of Geophysics*, *46*(3), RG3004. https://doi.org/10.1029/2007RG000227

Tual, L., Smit, M. A., Kooijman, E., Kielman-Schmitt, M., & Ratschbacher, L. (2022). Garnet, zircon, and monazite age and REE signatures in (ultra) high-temperature and high-pressure rocks: Examples from the Caledonides and the Pamir. *Journal of Metamorphic Geology*, *40*(8), 1321–1346. https://doi.org/10.1111/jmg.12667

van de Lagemaat, S. H. A., & van Hinsbergen, D. J. J. (2024). Plate tectonic cross-roads: Reconstructing the Panthalassa-Neotethys Junction Region from Philippine Sea Plate and Australasian oceans and orogens. *Gondwana Research*, *126*, 129–201. https://doi.org/10.1016/j.gr.2023.09.013

van Hinsbergen, D. J. J., Lippert, P. C., Li, S., Huang, W., Advokaat, E. L., & Spakman, W. (2019). Reconstructing Greater India: Paleogeographic, kinematic, and geodynamic perspectives. *Tectonophysics*, *760*, 69–94. https://doi.org/10.1016/j.tecto.2018.04.006

Vermeesch, P. (2018). IsoplotR: A free and open toolbox for geochronology. *Geoscience Frontiers*, *9*(5), 1479–1493. https://doi.org/10.1016/J.GSF.2018.04.001

Vry, J., & Baker, J. (2006). LA-MC-ICPMS Pb–Pb dating of rutile from slowly cooled granulites: Confirmation of the high closure temperature for Pb diffusion in rutile. *Geochimica et Cosmochimica Acta*, *70*(7), 1807–1820. https://doi.org/10.1016/j.gca.2005.12.006

Warnock, A. C., Zeitler, P. K., Wolf, R. A., & Bergman, S. C. (1997). An evaluation of low-temperature apatite UTh/He thermochronometry. *Geochimica et Cosmochimica Acta*, *61*(24), 5371–5377. https://doi.org/10.1016/S0016-7037(97)00302-5

Warren, C. J. (2013). Exhumation of (ultra-)high-pressure terranes: Concepts and mechanisms. *Solid Earth*, *4*(1), 75–92. https://doi.org/10.5194/se-4-75-2013

Warren, C. J., Beaumont, C., & Jamieson, R. A. (2008a). Formation and exhumation of ultra-high-pressure rocks during continental collision: Role of detachment in the subduction channel. *Geochemistry, Geophysics, Geosystems*, *9*(4), Q04019. https://doi.org/10.1029/2007GC001839

Warren, C. J., Beaumont, C., & Jamieson, R. A. (2008b). Modelling tectonic styles and ultra-high pressure (UHP) rock exhumation during the transition from oceanic subduction to continental collision. *Earth and Planetary Science Letters*, *267*(1), 129–145. https://doi.org/10.1016/j.epsl.2007.11.025

Warren, C. J., Beaumont, C., & Jamieson, R. A. (2008c). Deep subduction and rapid exhumation: Role of crustal strength and strain weakening in continental subduction and ultrahigh-pressure rock exhumation. *Tectonics*, *27*(6). https://doi.org/10.1029/2008TC002292

Waters, D. J. (2019). Metamorphic constraints on the tectonic evolution of the High Himalaya in Nepal: The art of the possible. *Geological Society, London, Special Publications*, *483*(1), 325–375. https://doi.org/10.1144/SP483-2018-187

Watson, E., Wark, D., & Thomas, J. (2006). Crystallization thermometers for zircon and rutile. *Contributions to Mineralogy and Petrology*, *151*(4), 413–433. https://doi.org/10.1007/s00410-006-0068-5

Wilke, F., O'Brien, P., Schmidt, A., & Ziemann, M. (2015). Subduction, peak and multi-stage exhumation metamorphism: Traces from one coesite-bearing eclogite, Tso Morari, western Himalaya. *Lithos*, *231*, 77–91. https://doi.org/10.1016/j.lithos.2015.06.007

Yamato, P., Burov, E., Agard, P., Le Pourhiet, L., & Jolivet, L. (2008). HP-UHP exhumation during slow continental subduction: Self-consistent thermodynamically and thermomechanically coupled model with application to the Western Alps. *Earth and Planetary Science Letters*, *271*(1–4), 63–74. https://doi.org/10.1016/j.epsl.2008.03.049

Zack, T., & Kooijman, E. (2017). Petrology and geochronology of rutile. *Reviews in Mineralogy and Geochemistry*, *83*(1), 443–467. https://doi.org/10.2138/rmg.2017.83.14

Zahirovic, S., Matthews, K. J., Flament, N., Müller, R. D., Hill, K. C., Seton, M., & Gurnis, M. (2016). Tectonic evolution and deep mantle structure of the eastern Tethys since the latest Jurassic. *Earth-Science Reviews*, *162*, 293–337. https://doi.org/10.1016/j.earscirev.2016.09.005

Zhang, D., Ding, L., Chen, Y., Schertl, H.-P., Qasim, M., Jadoon, U. K., et al. (2022). Two contrasting exhumation scenarios of deeply subducted continental crust in north Pakistan. *Geochemistry, Geophysics, Geosystems*, *23*(2), e2021GC010193. https://doi.org/10.1029/2021GC010193

Zhang, Z. M., Zhao, G. C., Santosh, M., Wang, J. L., Dong, X., & Liou, J. G. (2010). Two stages of granulite facies metamorphism in the eastern Himalayan syntaxis, South Tibet: Petrology, zircon geochronology and implications for the subduction of Neo-Tethys and the Indian continent beneath Asia. *Journal of Metamorphic Geology*, *28*(7), 719–733. https://doi.org/10.1111/j.1525-1314.2010.00885.x

Zhou, J., & Su, H. (2019). Site and timing of substantial India-Asia collision inferred from crustal volume budget. *Tectonics*, *38*(7), 2275–2290. https://doi.org/10.1029/2018TC005412

Zhu, D.-C., Wang, Q., Chung, S.-L., Cawood, P. A., & Zhao, Z.-D. (2019). Gangdese magmatism in southern Tibet and India–Asia convergence since 120 Ma. *Geological Society, London, Special Publications*, *483*(1), 583–604. https://doi.org/10.1144/SP483.14